

Nonlinear magnetotransport in a two-dimensional system with merging Dirac points

Ojasvi Pal¹, Bashab Dey^{1,2} and Tarun Kanti Ghosh¹

¹Department of Physics, Indian Institute of Technology-Kanpur, Kanpur-208016, India

²Institute for Theoretical Physics, University of Regensburg, Regensburg-93053, Germany

We study the linear, second-order nonlinear (NL) current and voltage responses of a two-dimensional gapped semi-Dirac system with merging Dirac nodes along the x direction under the influence of a weak magnetic field (B), using the semiclassical Boltzmann formalism. We investigate the effect of band geometric quantities like Berry curvature and orbital magnetic moment (OMM) in the responses up to linear order in B . We derive exact analytical expressions of the linear magnetoconductivities, second-harmonic NL anomalous Hall (NAH), and anomalous velocity and Lorentz force induced (NAL) conductivities, unveiling their dependence on Fermi energy and a gap parameter δ_0 . For $\delta_0 > 0$, the Fermi surface topology changes at a particular Fermi energy, which is reflected in the nature of conductivities through a kink. The ratio of NAL and NAH conductivities is found to be independent of δ_0 and inversely related to Fermi energy. The NL dc current exhibits distinct orientations depending on the Fermi energy, magnetic field, polarization of the electromagnetic wave. In the presence of magnetic field, the NL dc current vector can be rotated through large angles on variation of Fermi energy. For high Fermi energies, the NL dc current is directed nearly along the y -axis for x -polarized and low-frequency circularly polarized light, whereas it aligns close to x -axis for high-frequency circularly polarized light. These orientations of the NL dc current are predominantly governed by the mirror symmetry of the system along the x direction. Additionally, we also study the NL voltage responses of the system by applying current along the x and y directions. The system exhibits asymmetry in the B -dependencies of the NL resistivities for the two current directions, which may serve as an experimentally relevant signature for band geometric quantities and merging Dirac nodes in such systems.

I. INTRODUCTION

The exfoliation of graphene in 2004 marked an important epoch in the history of 2D materials due to its unique linear-Dirac spectrum and exotic transport properties^{1,2}. The two subbands of graphene touch at two inequivalent points in the reciprocal space named Dirac points, effectively describing the low-energy properties. These Dirac points can be manipulated by varying band parameters such as interaction strength and hopping amplitudes, resulting in the motion of Dirac points. Other two-dimensional physical systems with such spectrum have been observed in organic conductor α -(BEDT-TTF)₂I₃ under pressure³⁻⁶, 8- $Pmmn$ borophene⁷⁻⁹, artificially fabricated nanostructures¹⁰⁻¹⁴ and ultracold atoms^{15,16}.

Several studies discovered the merging of Dirac points in the electronic spectrum of two-dimensional systems^{17,18}. The merging of a pair of Dirac points into a single one shows the existence of a topological Lifshitz transition which marks the separation between the semimetallic phase with two disconnected Fermi surfaces and an insulating gapped phase. This also leads to special semi-Dirac dispersion hosting massive fermion behavior along one direction while massless Dirac characteristics in the orthogonal direction^{19,20}. It has been predicted that materials like TiO₂/VO₂ nanostructures under quantum confinement²¹ and dielectric photonic crystals²² can exhibit such low-energy dispersions. The merging of Dirac points has been observed experimentally in optical lattices²³, microwave cavities¹³ and recently, in potassium deposited few-layer black phosphorous²⁴. The transport properties

such as diffusion²⁵, optical conductivity²⁶⁻²⁹, formation of Landau levels spectra under magnetic field^{30,31}, magneto-optical conductivity³², dynamic polarization and plasmons³³ has been studied extensively for semi-Dirac systems. The Landau levels and transport properties for a semi-Dirac nanoribbon were discussed in recent work³⁴. Very recent studies probed the topological phases of a Chern insulator in such systems by tuning the strength of a circularly polarized light³⁵ and in the presence of extended range hopping³⁶.

The topological behavior of the bands is manifested in the Berry curvature and OMM of the electrons which can significantly affect the linear and the NL transport properties^{37,38}. Some well-known examples in the linear response regime are anomalous Hall effect³⁹⁻⁴¹, anomalous thermal Hall effect^{42,43}, planar Hall effect^{44,45}, magnetoresistance^{46,47}. The discovery of the NL anomalous Hall effect induced by the Berry curvature dipole⁴⁸ in the time-reversal symmetric (TRS) system accelerated the investigation of other NL transport phenomena⁴⁹⁻⁵⁷. Moreover, it has been realized that such NL transport responses in 2D Dirac systems survive either in the presence of spin-orbit coupling which results in tilting of the Dirac cone, or higher order warping of the Fermi surface^{48,58}. Recent studies reveal that the low-energy Hamiltonian that features a pair of Dirac points separated by a saddle point or the merging of two Dirac points can give rise to Berry curvature dipole induced NL transport properties⁵⁹. However, the linear and NL current responses of such systems in the presence of a magnetic field are not explored.

In this work, we calculate the contribution of Berry

curvature and OMM to the linear and NL conductivities in the presence of a weak magnetic field, using the Boltzmann approach. We also study the second-order NL magnetoresistivity of the system for two different orientations of the applied current. The anisotropy in the nature of B -dependencies of the NL resistivities may act as an experimental probe for band geometric quantities as well as merging Dirac nodes in these systems.

This paper is structured as follows: In Sec. II, we present the general formulas to calculate the second-order NL current responses in the presence of a weak magnetic field. In particular, we discuss the contribution of Berry curvature and OMM to the NL magnetoconductivities. In Sec. III, we provide a discussion on the 2D gapped semi-Dirac model with merging Dirac nodes. In Sec. IV, we present the results of linear and NL magnetoconductivities. We further analyze our results and discuss the dependence of all the contributions on Fermi energy and other system parameters in its subsequent subsections. We also discuss the orientations of NL DC current in response to the linearly and circularly polarized light. Section V is dedicated to the discussion of the second-order NL voltage responses. Finally, we summarize our main results in Sec. VI.

II. THEORETICAL FORMULATION

In this section, we provide the general formalism to calculate the second-order NL current responses in presence of the electric field which oscillates in time but uniform in space, $\mathbf{E}(t) = \text{Re}[\mathbf{E}e^{-i\omega t}] = (1/2)[\mathbf{E}e^{-i\omega t} + \mathbf{E}^*e^{i\omega t}]$ with $\mathbf{E} = E_x\hat{x} + E_y\hat{y}$, where $E_x, E_y \in \mathbb{C}$ and a static magnetic field \mathbf{B} . Theoretically, for an applied electric field $\mathbf{E}(t)$, the linear current of fundamental frequency $j_a^\omega = \sigma_{ab}E_b$ and the NL current $j_a^{\text{NL}} = \text{Re}[j_a^{(0)} + j_a^{(2\omega)}e^{-2i\omega t}]$ are measured. Here, $j_a^{(0)} = \chi_{abc}^{(0)}E_bE_c^*$ describes the NL DC current and $j_a^{(2\omega)} = \chi_{abc}^{(2\omega)}E_bE_c$ describes the second-harmonic (SH) current and the subscript a, b and c are the coordinate indices.

The charge current is defined as $\mathbf{j}(t) = -e \int [d\mathbf{k}] D_{\mathbf{k}} \dot{\mathbf{r}} f(t)$, where $[d\mathbf{k}] = d^2k/(2\pi)^2$, $f(t)$ denotes the nonequilibrium distribution function (NDF), $D_{\mathbf{k}} = [1 + (e/\hbar)(\mathbf{B} \cdot \boldsymbol{\Omega})]$ is the phase-space modifying factor³⁷ with $\boldsymbol{\Omega}$ as the Berry curvature. For simplicity, hereafter we will denote $D_{\mathbf{k}}$ by D , omitting the implied k dependence. The modified semiclassical equations of motion (including Berry curvature and OMM) for the configuration $(\mathbf{E} \perp \mathbf{B})$ are given by^{37,60,61}

$$\dot{\mathbf{r}} = \frac{1}{D} \left[\tilde{\mathbf{v}}_{\mathbf{k}} + \frac{e}{\hbar} (\mathbf{E}(t) \times \boldsymbol{\Omega}) \right], \quad (1)$$

$$\hbar \dot{\mathbf{k}} = \frac{1}{D} \left[-e\mathbf{E}(t) - e(\tilde{\mathbf{v}}_{\mathbf{k}} \times \mathbf{B}) \right]. \quad (2)$$

The semiclassical band velocity is defined as $\hbar \tilde{\mathbf{v}}_{\mathbf{k}} = \nabla_{\mathbf{k}} \tilde{\epsilon}_{\mathbf{k}}$, where $\tilde{\epsilon}_{\mathbf{k}} = \epsilon_{\mathbf{k}} - \epsilon_{\mathbf{k}}^m$ is the modified band energy due to

Zeeman-like coupling of OMM with the external magnetic field. The OMM modified velocity can be expressed as $\tilde{\mathbf{v}}_{\mathbf{k}} = \mathbf{v}_{\mathbf{k}} - \mathbf{v}_{\mathbf{k}}^m$ with $\hbar \mathbf{v}_{\mathbf{k}}^m = \nabla_{\mathbf{k}}(\mathbf{m} \cdot \mathbf{B})$. The Berry curvature for the n -th band can be computed using $\boldsymbol{\Omega}^n = -\text{Im}[(\nabla_{\mathbf{k}} u_{\mathbf{k}}^n | \times | \nabla_{\mathbf{k}} u_{\mathbf{k}}^n \rangle)]$, where $|u_{\mathbf{k}}^n\rangle$ is the unperturbed eigenstate^{37,62}. The OMM, generated by the semiclassical self-rotation of the Bloch wave packet, can be evaluated using $\mathbf{m}^n = -(e/2\hbar)\text{Im}[(\nabla_{\mathbf{k}} u_{\mathbf{k}}^n | \times (H - \epsilon_{\mathbf{k}}^n) | \nabla_{\mathbf{k}} u_{\mathbf{k}}^n \rangle]$ ⁶³. The Boltzmann transport equation within the relaxation time approximation to obtain the non-equilibrium distribution function (NDF) $f(t)$ is given by⁶⁴

$$\frac{\partial f(t)}{\partial t} + \dot{\mathbf{k}} \cdot \nabla_{\mathbf{k}} f(t) = -\frac{f(t) - \tilde{f}_{\text{eq}}}{\tau}. \quad (3)$$

Here, $\tilde{f}_{\text{eq}} = [1 + e^{\beta(\tilde{\epsilon}_{\mathbf{k}} - \mu)}]^{-1}$ is the Fermi-Dirac distribution function and τ is the relaxation time which is considered constant (energy independent) in our case. The NDF can be expressed as $f(t) = \tilde{f}_{\text{eq}} + \sum_{n=1}^{\infty} f_n(t)$, where the non-equilibrium part of the NDF can be understood as a power series of the electric field i.e., $f_n \propto E^n$. The recursive equation of f_n can be obtained from Eq. (3) to get the NDF up to quadratic order in an electric field. The general expressions of the linear response current are discussed in details in Appendix A and the corresponding nonzero linear conductivities are given by Eqs. (A3), (A6)-(A7). These linear conductivities do not have an explicit role in the NL conductivities, but are used to calculate the NL resistivities, which will be discussed in a later section.

Second-order nonlinear current responses

To calculate the second-order NL current responses quadratic in E and up to linear order in B , we consider the ansatz for NDF quadratic in E ,

$$f_2(t) = f_2^0 + f_2^{0*} + f_2^{2\omega} e^{-i2\omega t} + f_2^{2\omega*} e^{i2\omega t}, \quad (4)$$

where f_2^0 denotes the rectification (dc) part and $f_2^{2\omega}$ denotes the SH part of the NDF. Substituting it in Eq. (3) and applying the Zener-Jones method⁶⁵, we can express $f_2^{2\omega}$ in terms of the infinite series of Lorentz force operator $\hat{L}_B = (e/\hbar)[(\tilde{\mathbf{v}}_{\mathbf{k}} \times \mathbf{B}) \cdot \nabla_{\mathbf{k}}]$ as⁶⁶

$$f_2^{2\omega} = \frac{1}{2} \sum_{\eta=0}^{\infty} \left(\frac{\tau_{2\omega} \hat{L}_B}{D} \right)^{\eta} \left(\frac{e\tau_{2\omega}}{\hbar D} \mathbf{E} \cdot \nabla_{\mathbf{k}} f_1^{\omega} \right), \quad (5)$$

where $\tau_{2\omega} = \tau/(1 - 2i\omega\tau)$ and $f_2^0 = f_2^{2\omega}(\mathbf{E} \rightarrow \mathbf{E}^*, \tau_{2\omega} \rightarrow \tau)$. Here, f_1^{ω} is the first-order correction to the distribution function which is presented in Appendix A. Taking into account the weak B -field strength, we can express Eq. (5) as a power series of the magnetic field⁶¹. The equilibrium part of NDF \tilde{f}_{eq} consists of B -dependence through OMM-modified energy, thus it can be expanded via Taylor expansion in terms of B as $\tilde{f}_{\text{eq}} = f_{\text{eq}} - \epsilon_m f'_{\text{eq}}$, where $f'_{\text{eq}} \equiv \partial f_{\text{eq}}/\partial \epsilon_k$ with f_{eq} defined at $B = 0$.

A. Second-harmonic current

For an external electric field oscillating at frequency ω , we study the SH current generated at twice the excitation frequency, $j_a^{2\omega} = \chi_{abc}^{(2\omega)} E_b E_c$. The SH current can be written as $\mathbf{j}_2(t) = \mathbf{j}_{20}(t) + \mathbf{j}_{21}(t)$, where the first and second subscript represents the order of E and B respectively. The magnetic field independent SH current can be further expressed as $\mathbf{j}_{20}(t) = \mathbf{j}_{20}^{2\omega} e^{-2i\omega t} + \mathbf{j}_{20}^{2\omega*} e^{2i\omega t}$, where we obtain

$$\mathbf{j}_{20}^{2\omega} = \frac{-e^3 \tau_\omega}{4\hbar} \int [d\mathbf{k}] \left[(\mathbf{E} \times \boldsymbol{\Omega}) + \tau_{2\omega} \mathbf{v}_\mathbf{k} (\mathbf{E} \cdot \nabla_\mathbf{k}) \right] (\mathbf{E} \cdot \mathbf{v}_\mathbf{k}) f'_{\text{eq}}. \quad (6)$$

The corresponding nonzero SH conductivity is given by

$$\chi_{abc}^{(\text{NAH})} = -\frac{e^3 \tau_\omega}{4\hbar} \varepsilon_{abd} \int [d\mathbf{k}] \Omega_d v_c f'_{\text{eq}}. \quad (7)$$

Here, ε_{abd} is the Levi-Civita symbol and $abd \in xyz$. The

above equation denotes the SH anomalous Hall conductivity $\chi_{abc}^{(\text{NAH})}$ which is proportional to the dipole moment of Berry curvature over occupied states, defined as $\zeta_{bd} = -\int [d\mathbf{k}] (\nabla_{k_b} \epsilon_\mathbf{k}) \Omega_d f'_{\text{eq}}$. It is evident from the expression that Berry curvature dipole moment survives in time-reversal symmetric and inversion symmetry broken system, unlike the linear anomalous Hall conductivity. The second term in Eq. (6) corresponds to SH Drude conductivity (originating from band velocity) calculated as $\chi_{abc}^{(\text{D})} = -(e^3 \tau_\omega \tau_{2\omega} / 4\hbar) \int [d\mathbf{k}] v_a \partial_{k_b} v_c f'_{\text{eq}}$. The SH Drude conductivity vanishes if either of the symmetries between TRS and space inversion symmetry is present in contrast to linear Drude conductivity which is always nonzero.

The SH current linearly dependent on the magnetic field can be written as $\mathbf{j}_{21}(t) = \mathbf{j}_{21}^{2\omega} e^{-2i\omega t} + \mathbf{j}_{21}^{2\omega*} e^{2i\omega t}$, where

$$\begin{aligned} \mathbf{j}_{21}^{2\omega} = \frac{e^3}{4\hbar} \int [d\mathbf{k}] \left\{ (\mathbf{E} \times \boldsymbol{\Omega}) \left[-\tau_\omega^2 \hat{L} (\mathbf{E} \cdot \mathbf{v}_\mathbf{k}) f'_{\text{eq}} \right] + \tau_\omega \tau_{2\omega} \mathbf{v}_\mathbf{k} \mathbf{E} \cdot \left[\frac{e}{\hbar} (\boldsymbol{\Omega} \cdot \mathbf{B}) \nabla_\mathbf{k} (\mathbf{E} \cdot \mathbf{v}_\mathbf{k} f'_{\text{eq}}) + \nabla_\mathbf{k} \left(\frac{e}{\hbar} (\boldsymbol{\Omega} \cdot \mathbf{B}) (\mathbf{E} \cdot \mathbf{v}_\mathbf{k}) f'_{\text{eq}} \right) \right] \right. \\ \left. + \tau_\omega \tau_{2\omega} \left[\mathbf{v}_\mathbf{k} \mathbf{E} \cdot \nabla_\mathbf{k} (\mathbf{E} \cdot (\mathbf{v}_\mathbf{k}^m f'_{\text{eq}} + \epsilon_m \mathbf{v}_\mathbf{k} f''_{\text{eq}})) \right] + \mathbf{v}_\mathbf{k}^m \mathbf{E} \cdot \nabla_\mathbf{k} (\mathbf{E} \cdot \mathbf{v}_\mathbf{k} f'_{\text{eq}}) \right] \right\}. \end{aligned} \quad (8)$$

The finite contribution for the SH current linear in B is proportional to τ^2 , since terms $\propto \tau$ and τ^3 vanish due to TRS. It is to be noted that in the presence of SIS but broken TRS, all these contributions vanish. Therefore breaking of SIS elicit these nonzero SH responses. The SH conductivity in the presence of a magnetic field encompasses three distinct contributions: the combined effects of anomalous velocity and Lorentz force, the OMM, and the Berry curvature correction to the phase-space factor. The SH Hall conductivity emerging from the combined effects of anomalous velocity and Lorentz force $\chi_{abc}^{(\text{NAL})}$ can be obtained as

$$\chi_{abc}^{(\text{NAL})} = \frac{e^4 \tau_\omega^2 B}{4\hbar^2} \varepsilon_{abd} \int [d\mathbf{k}] \Omega_d (\mathbf{v}_\mathbf{k} \times \nabla_\mathbf{k})_z (v_c f'_{\text{eq}}). \quad (9)$$

The SH conductivity incited by OMM is given by

$$\begin{aligned} \chi_{abc}^{(\text{OMM})} = \frac{e^3 \tau_\omega \tau_{2\omega}}{4\hbar} \int [d\mathbf{k}] \left[v_{ma} \partial_{k_b} (v_c f'_{\text{eq}}) \right. \\ \left. + v_a \partial_{k_b} (v_{mc} f'_{\text{eq}} + \epsilon_m v_c f''_{\text{eq}}) \right]. \end{aligned} \quad (10)$$

Here, f''_{eq} is the double derivative of f_{eq} w.r.t energy. The contribution to the SH conductivity generated by the phase-space factor is obtained as

$$\chi_{abc}^{(\text{B})} = \frac{e^4 \tau_\omega \tau_{2\omega}}{4\hbar^2} \int [d\mathbf{k}] v_a [(\boldsymbol{\Omega} \cdot \mathbf{B}) \partial_{k_b} + \partial_{k_b} (\boldsymbol{\Omega} \cdot \mathbf{B})] v_c f'_{\text{eq}}. \quad (11)$$

We emphasize that all the above three contributions to the SH conductivities in the presence of a magnetic field depend on intrinsic band geometric quantities, namely Berry curvature and OMM.

B. Nonlinear DC current

The second-order response also includes a zero-frequency current known as the photogalvanic effect (PGE). The NL dc current can be expressed as $j_a^{(0)} = \chi_{abc}^{(0)} E_b E_c^*$.

The NL dc current arising from the anomalous velocity of Bloch electrons (without magnetic field) can be obtained as³⁸

$$\begin{aligned} \mathbf{j}_{\text{NAH}}^{(0)} = \frac{1}{1 + \omega^2 \tau^2} \left[2 \left(\chi_{xyy,0}^{(\text{NAH})} |E_y|^2 \hat{\mathbf{x}} + \chi_{yxx,0}^{(\text{NAH})} |E_x|^2 \hat{\mathbf{y}} \right) \right. \\ \left. + \left(\chi_{xyx,0}^{(\text{NAH})} [E_y E_x^*]_+ \hat{\mathbf{x}} + \chi_{yxy,0}^{(\text{NAH})} [E_y E_x^*]_+ \hat{\mathbf{y}} \right) \right. \\ \left. - i\omega \tau \left(\chi_{xyx,0}^{(\text{NAH})} [E_y E_x^*]_- \hat{\mathbf{x}} - \chi_{yxy,0}^{(\text{NAH})} [E_y E_x^*]_- \hat{\mathbf{y}} \right) \right], \end{aligned} \quad (12)$$

where $[E_b E_c^*]_\pm = E_b E_c^* \pm E_c E_b^*$ and $\chi_{abc,0}^{(\text{NAH})} = \chi_{abc}^{(\text{NAH})}(\omega = 0)$ represents the SH anomalous Hall conductivity given by Eq. (7) at $\omega = 0$. In Eq. (12), the terms in the first parentheses denote the typical photovoltaic effect and the terms in the second (third) parentheses describe the linear (circular) PGE. On the variation of the polarization, the linear PGE (LPGE) is maximum for linearly polarized light, whereas the circular PGE (CPGE)

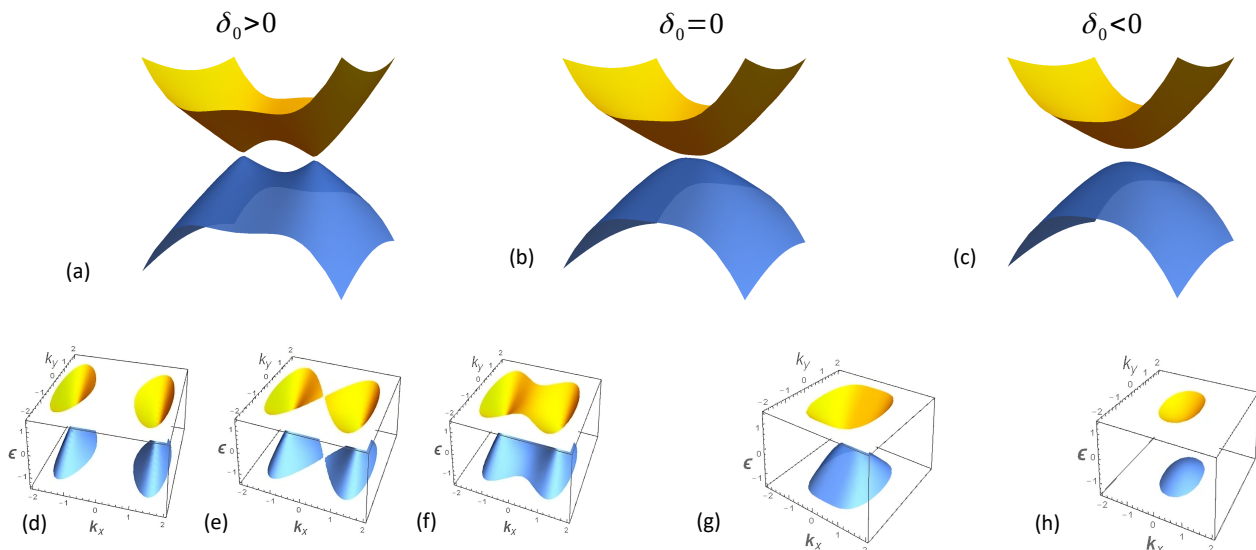


FIG. 1: Top panel (a)-(c) represents the energy spectrum of the model given by Eq. (13) for different values of gap parameter δ_0 . Plot (a) shows the case of $\delta_0 > 0$ describing the phase with two Dirac nodes separated by $2\sqrt{\delta_0/\alpha}$ distance along k_x direction, (b) $\delta_0 = 0$ corresponds to the semi-Dirac form where two Dirac nodes merge and (c) represents the gapped phase. Bottom panel (d)-(h) illustrates the constant Fermi energy contours corresponding to different values of δ_0 and Fermi energy. (d)-(f) describes the energy contours existing for three scenarios when $\delta_0 > 0$. (d) represent the two disconnected Fermi surfaces in accordance with the two distinct Dirac nodes till $\delta_0 > \sqrt{\mu^2 - m_0^2}$, (e) the two Fermi surfaces get connected by a saddle point at $\delta_0 = \sqrt{\mu^2 - m_0^2}$ and (f) the single connected Fermi surface exists as long as $\delta_0 < \sqrt{\mu^2 - m_0^2}$. (g) and (h) describes the constant Fermi energy contours for $\delta_0 = 0$ and $\delta_0 < 0$ respectively. Here, we have used $\beta = 10^5$ m/s, $m_0 = 0.1$ eV, $\alpha = 2.7$ meV·nm² with $m^* = 13.6 m_e$ for $(\text{TiO}_2)_5/(\text{VO}_2)_3$, where m_e is the free electron mass.

is maximum for circularly polarized light. The CPGE current reverses sign when polarization state of the electric field changes from left to right circular. Note that the LPGE vanishes for circularly polarized light, whereas the CPGE vanishes for linearly polarized light. In Appendix B, we present the general formulas for various contributions arising from the geometric quantities to the NL DC current in the presence of a magnetic field. These contributions are expressed in terms of the polarization of the electromagnetic wave.

In the upcoming sections, we will apply this formalism to the semi-Dirac model with the merging Dirac nodes and investigate its linear and second-order NL transport properties in the presence of a low B -field.

III. GAPPED SEMI-DIRAC SYSTEM

The low-energy Hamiltonian that describes the merging of two Dirac nodes has the following form^{20,25,59}

$$H(\mathbf{k}) = (\alpha k_x^2 - \delta_0)\sigma_x + \hbar\beta k_y\sigma_y + m_0\sigma_z, \quad (13)$$

where $\boldsymbol{\sigma} = (\sigma_x, \sigma_y, \sigma_z)$ are the 2×2 Pauli matrices in pseudospin space, \mathbf{k} is the crystal momentum having magnitude, $k = \sqrt{k_x^2 + k_y^2}$, δ_0 and m_0 are the gap parameter, $\alpha = \hbar^2/2m^*$ with m^* as effective mass related

to the x -direction and β is the Dirac velocity along the y -direction. In the Hamiltonian given by Eq. (13), the mirror symmetry is preserved along the x direction and broken along the y direction. The energy spectrum is given by

$$\epsilon_\lambda(\mathbf{k}) = \lambda\sqrt{(\alpha k_x^2 - \delta_0)^2 + \hbar^2\beta^2 k_y^2 + m_0^2}, \quad (14)$$

where $\lambda = \pm$ denotes the conduction and valence band respectively. The corresponding band dispersion is shown in Fig. 1. The x -component of semiclassical band velocity is calculated as $\hbar v_x = 2\alpha k_x(\alpha k_x^2 - \delta_0)/\epsilon_{\mathbf{k}}$ and its y -component is $v_y = \hbar\beta^2 k_y/\epsilon_{\mathbf{k}}$. Equation (13) has been termed the ‘‘Universal Hamiltonian’’ as different types of the spectrum can be obtained by tuning the gap parameter δ_0 ²⁰. The Hamiltonian with $\delta_0 > 0$ describes the phase that consists of two Dirac nodes separated by $2\sqrt{\delta_0/\alpha}$ distance along the k_x axis. In the limit of $\delta_0 = 0$, the two Dirac nodes merge and the resulting dispersion exhibits semi-Dirac behavior which is quadratic in the x -direction and linear in the y -direction. For $\delta_0 < 0$, a trivial insulating phase is obtained with a nonzero energy gap. Thus the variation of parameter δ_0 from negative to positive values drives the transition from an insulating phase to a semi-metallic phase. The mass term $m_0\sigma_z$ is added in the Hamiltonian to introduce an energy gap at the Dirac nodes.

We employ the method of parameterization to the con-

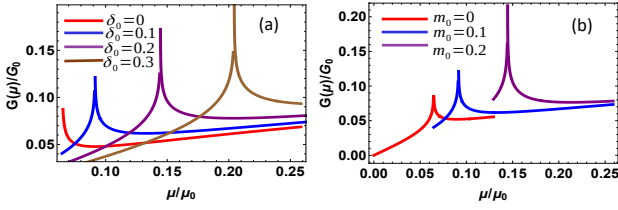


FIG. 2: Variation of the density of states as a function of Fermi energy: (a) at fixed $m_0 = 0.1$ eV for different values of δ_0 (in eV) and (b) at fixed $\delta_0 = 0.1$ eV for given values of m_0 (in eV). The normalization parameters for density of states and Fermi energy are $G_0 = 1/\alpha$ and $\mu_0 = \hbar^2 \beta^2 / \alpha$ respectively. The parameters used are the same as in Fig. 1.

stant energy contours $\epsilon(\mathbf{k})$ in Eq. (14) considering the sign of k_x ($k_x \leq 0$) in each half-plane. The change of coordinates goes as $\alpha k_x^2 - \delta_0 = r \cos \phi$, $\hbar \beta k_y = r \sin \phi$ and $\varsigma_k = \text{sgn}(k_x) = \pm 25$. The energy spectrum now acquires the simplified form, $\epsilon_{\mathbf{k}} = \pm \sqrt{r^2 + m_0^2}$ and ϕ represents the coordinate along the constant energy contour. The limit of ϕ varies according to the topology of the constant energy contours obtained for different energies. The eigenstates are given by

$$\psi_{\mathbf{k}}^{\pm}(\mathbf{r}) = e^{i\mathbf{k}\cdot\mathbf{r}} \begin{pmatrix} \pm r \\ \sqrt{r^2 + (\sqrt{r^2 + m_0^2} \mp m_0)^2} \\ (\sqrt{r^2 + m_0^2} \mp m_0) e^{i\phi} \\ \sqrt{r^2 + (\sqrt{r^2 + m_0^2} \mp m_0)^2} \end{pmatrix}. \quad (15)$$

Next, we discuss the constant Fermi energy contours

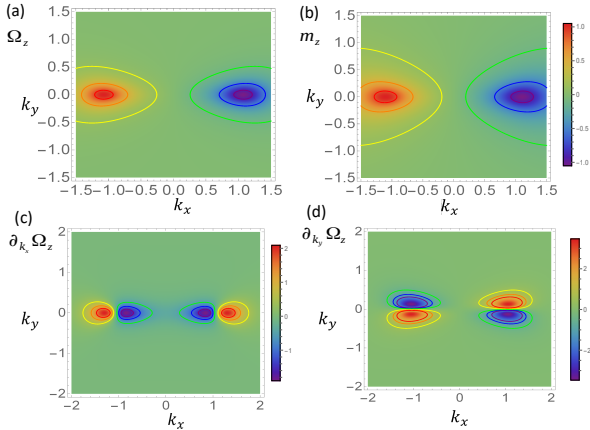


FIG. 3: Density-contour plot of (a) Berry curvature (in units of 10^{-1} nm^2), (b) OMM (in units of $4 \alpha e/\hbar$), (c) and (d) derivative of Berry curvature with respect to k_x and k_y respectively for the conduction band of the system. Here, k_x and k_y are plotted in units of $\sqrt{\delta_0/\alpha}$. The parameters used are the same as in Fig. 1.

corresponding to different values of δ_0 and Fermi energy. For a given Fermi energy in the conduction band, the band contains only one minima at $\delta_0 = 0$. Hence, we

get a single Fermi surface as a result of one nodal point (semi-Dirac node). When δ_0 starts to increase, the single minima splits into two minima giving rise to two allowed wave vectors that correspond to two distinct Dirac nodes with linear dispersion. A single connected Fermi surface continues to exist till $\delta_0 < \sqrt{\mu^2 - m_0^2}$ and the area of the Fermi surface gets enhanced due to the presence of extra curvature emerging from the splitting of single minima. These two Dirac points are connected by a saddle point which on a further increase of δ_0 yield two connected Fermi surfaces at $\delta_0 = \sqrt{\mu^2 - m_0^2}$. The two disconnected Fermi surfaces are formed for $\delta_0 > \sqrt{\mu^2 - m_0^2}$ which marks the onset of a decrease in the Fermi surface area since the bands get narrower with the increase of δ_0 . The Fermi surface topology nearly remains uninterrupted with δ_0 for high Fermi energy. Thus the range of $\phi \in [-\phi_0, \phi_0]$ can be separated into two regions for the case of $\delta_0 > 0$,

$$\phi_0 = \begin{cases} \arccos \left[\frac{-\delta_0}{\sqrt{\mu^2 - m_0^2}} \right], & \delta_0 < \sqrt{\mu^2 - m_0^2}, \\ \pi, & \delta_0 \geq \sqrt{\mu^2 - m_0^2}. \end{cases} \quad (16)$$

The Jacobian for the transformation of coordinates from (k_x, k_y) to (r, ϕ) is given by

$$J(r, \phi) = \frac{r}{2\hbar\beta\sqrt{\alpha(r \cos \phi + \delta_0)}}. \quad (17)$$

We obtain the density of states (DOS) given as

$$G(\mu) = 2 \frac{G_0}{\pi^2 \sqrt{8}} \sqrt{\frac{\tilde{\delta}_0^2 + \tilde{m}_0^2 \gamma^2}{\gamma \tilde{\delta}_0}} \begin{cases} K(k), & \gamma < 1, \\ k' [K(k')], & \gamma \geq 1, \end{cases} \quad (18)$$

where $K(k)$ and $E(k)$ are the complete elliptic integrals of the first and second kind, respectively, with $k = \sqrt{(1+\gamma)/2}$ and $k' = 1/k = \sqrt{2/(1+\gamma)}$ known as the modulus of Jacobian elliptic function and integrals. We introduce $\gamma = \delta_0/\sqrt{\mu^2 - m_0^2}$ as a reduced parameter and $G_0 = 1/\alpha$. Note that an overall factor of 2 is multiplied to consider the sign of k_x . Here, we define the scaled system parameters as $\tilde{\delta}_0 = \delta_0/\mu_0$ and $\tilde{m}_0 = m_0/\mu_0$ with $\mu_0 = \hbar^2 \beta^2 / \alpha$. We choose $\mu > m_0$ such that the Fermi energy lies above the bulk gap. Expanding the above expression of DOS for $\gamma \geq 1$ up to leading order in k' gives

$$G(\mu) \simeq \frac{G_0}{32\pi} \sqrt{\frac{\tilde{\delta}_0^2 + \tilde{m}_0^2 \gamma^2}{\gamma \tilde{\delta}_0}} \left(\frac{33 + 40\gamma + 16\gamma^2}{(1+\gamma)^{5/2}} \right). \quad (19)$$

Near the band-edge in the limit of $\gamma \rightarrow \infty$, $G(\mu) \propto 1/\sqrt{\delta_0}$. For very low doping, DOS decreases with δ_0 whereas, for high doping, DOS increases with δ_0 and matches with semi-Dirac result in the large μ limit as shown in Fig. 2(a). Note that divergence occurs exactly at the saddle point ($\gamma = 1$). Equation 18 at $m_0 = 0$ reduces to the known results²⁰. We also plotted the variation of DOS with Fermi energy at fixed $\delta_0 = 0.1$ eV for

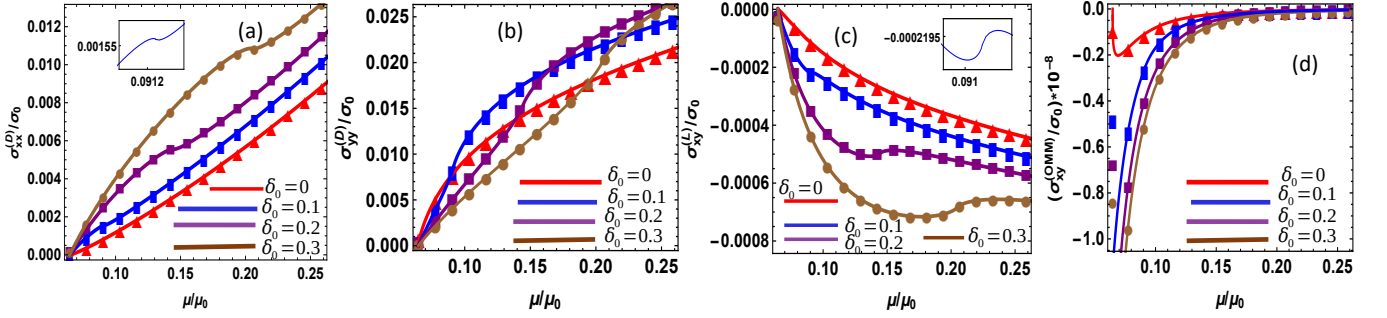


FIG. 4: Variation of linear conductivities (up to linear order in B) with the Fermi energy for different values of δ_0 (in eV). (a)-(b) Drude conductivity along the x and y direction respectively, (c) Lorentz force induced linear Hall conductivity, and (d) OMM induced linear Hall conductivity. The normalization parameter for linear conductivities is $\sigma_0 = \tau e^2 \beta^2 / \alpha$. Here, the solid color curves represent the results of analytical calculations at zero temperature whereas the corresponding colored plot markers are the representatives of the results of numerical calculations performed at temperature $T = 34$ K. The inset is a blow-up of the region around $\mu = \sqrt{\delta_0^2 + m_0^2}$ for $\delta_0 = 0.1$ eV. The parameters used are $\beta = 10^5$ m/s, $\alpha = 2.7$ meV \cdot nm 2 with $m^* = 13.6m_e$, $\tau = 10^{-12}$ s, $B = 2$ T and $m_0 = 0.1$ eV.

different values of energy gap parameter m_0 in Fig. 2(b). We find that as we increase the value of m_0 from 0.0 to 0.1 eV, the peak of divergence also gets shifted since the allowed range of μ will also change from $\mu = 0.0$ to 0.1 eV such that $\mu > m_0$ to get the physical results.

The Berry curvature and OMM of the given Hamiltonian can be calculated as

$$\Omega_z = \mp \frac{\hbar \alpha \beta m_0 k_x}{\epsilon_{\mathbf{k}}^3}, \quad m_z = -\frac{e \alpha \beta m_0 k_x}{\epsilon_{\mathbf{k}}^2}. \quad (20)$$

It is to be noted that Berry curvature and OMM are zero for the gapless system ($m_0 = 0$), whereas, in the limit of $\delta_0 = 0$, it remains nonzero. The OMM is the same for both the bands. The density-contour plot of the Berry curvature and OMM for the conduction band are shown in Fig. 3. The magnitude of Berry curvature decays rapidly as compared to OMM when Fermi energy shifts away from the band edge.

IV. RESULTS AND DISCUSSIONS

In this section, we calculate the linear, SH and NL dc current responses of the gapped semi-Dirac system in the presence of a static magnetic field applied along the z direction. In experimental setups^{50,67}, the ac frequency lies in the range of 10 – 1000 Hz and relaxation time $\tau \sim 10^{-12}$ s, which explains the transport limit, i.e., $\omega\tau \ll 1$. In this limit, $\tau_\omega \rightarrow \tau$ and $\tau_{2\omega} \rightarrow \tau$. In our work, we utilize this limit to determine the linear and SH conductivities of the system by substituting τ_ω and $\tau_{2\omega}$ with τ . In this limit, it is noteworthy that the SH and the NL DC conductivities are nearly equal.

Linear conductivities

We first evaluate the linear conductivities of the system using the general form of the Eqs. (A3), (A6)-(A7) along with modified coordinates that account for the dispersion anisotropy. In the limit of zero temperature, a derivative of the Fermi-Dirac distribution function is substituted by the Dirac-delta function which allows to perform the integral over energy analytically. Next, we can evaluate the angular integration by considering the appropriate limits of ϕ in accordance with the two regimes discussed in Eq. (16) for $\delta_0 > 0$. Such angular integrals can be expressed in terms of complete elliptic integrals of the first and second kinds. The xx -component of Drude conductivity can be calculated using Eq. (A3) as

$$\sigma_{xx}^{(D)} = \frac{\sqrt{2}\sigma_0}{15\pi^2} \frac{\tilde{\delta}_0^{5/2}}{\sqrt{\gamma^3(\tilde{\delta}_0^2 + \tilde{m}_0^2\gamma^2)}} \begin{cases} [(2\gamma^2 + 7\gamma - 9)K(k) + 2(9 - 2\gamma^2)E(k)], & \gamma < 1, \\ 2k[(9 - 2\gamma^2)E(k') + 2\gamma(\gamma - 1)K(k')], & \gamma \geq 1, \end{cases} \quad (21)$$

where $\sigma_0 = \tau e^2 \beta^2 / \alpha$. In view of anisotropic dispersion, $\sigma_{xx}^{(D)} \neq \sigma_{yy}^{(D)}$. Following the details of calculation similar to xx -term, the yy -component of Drude conductivity is calculated to be

$$\sigma_{yy}^{(D)} = \frac{\sqrt{2}\sigma_0}{6\pi^2} \frac{\tilde{\delta}_0^{3/2}}{\sqrt{\gamma(\tilde{\delta}_0^2 + \tilde{m}_0^2\gamma^2)}} \begin{cases} [2\gamma E(k) + (1 - \gamma)K(k)], & \gamma < 1, \\ 2k[\gamma E(k') - (\gamma - 1)K(k')], & \gamma \geq 1. \end{cases} \quad (22)$$

We have plotted the Drude conductivities $\sigma_{xx}^{(D)}$ and $\sigma_{yy}^{(D)}$ as a function of Fermi energy at the given values of δ_0 in Figs. 4(a) and 4(b). The behavior of conductivities is expectedly different for $\gamma < 1$ (high Fermi energy with

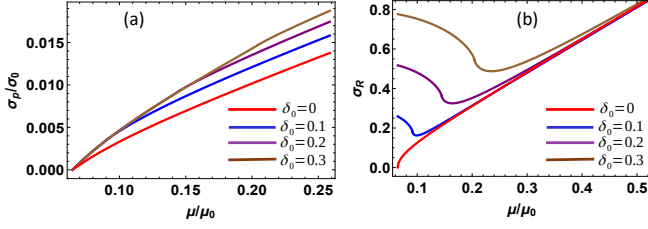


FIG. 5: (a)-(b) Plots of variation of $\sigma_P \equiv \sqrt{\sigma_{xx}^{(D)} \sigma_{yy}^{(D)}}$ and $\sigma_R \equiv \sigma_{xx}^{(D)}/\sigma_{yy}^{(D)}$ with the Fermi energy for different values of δ_0 (in eV). The solid color curves represent the analytical results calculated at zero temperature. All parameters used are the same as in Fig. 4.

single-connected Fermi surface) and $\gamma \geq 1$ (low Fermi energy with two Fermi surfaces) due to the particular Fermi surface topology in the two regimes. For the case of $\gamma \geq 1$, expanding the exact analytic expressions given by Eqs. (21) and (22) up to leading order in k' , we get

$$\begin{aligned} \sigma_{xx}^{(D)} &\simeq \frac{\sigma_0}{16\pi} \frac{\tilde{\delta}_0^{5/2}}{\sqrt{\gamma^3(\tilde{\delta}_0^2 + \tilde{m}_0^2\gamma^2)}} \left[\frac{(1+2\gamma)(3+4\gamma)}{(\gamma+1)^{3/2}} \right], \\ \sigma_{yy}^{(D)} &\simeq \frac{\sigma_0}{32\pi} \frac{\tilde{\delta}_0^{3/2}}{\sqrt{\gamma(\tilde{\delta}_0^2 + \tilde{m}_0^2\gamma^2)}} \left[\frac{(11+4\gamma)}{(\gamma+1)^{3/2}} \right]. \end{aligned} \quad (23)$$

In the limit of $\gamma \rightarrow \infty$ (near the band edge approximation i.e., $\mu \rightarrow m_0$), we find that $\sigma_{xx}^{(D)} \propto \mu^2 \sqrt{\delta_0}$ and $\sigma_{yy}^{(D)} \propto \mu^2 / \sqrt{\delta_0}$. Hence, for low doping, $\sigma_{xx}^{(D)}$ increases with both μ and δ_0 , whereas $\sigma_{yy}^{(D)}$ increases with the Fermi energy but decreases with δ_0 . We noticed a small kink in both the Drude conductivities as a consequence of a change in Fermi surface topology exactly at the saddle point ($\gamma = 1$) for the fixed positive values of δ_0 . For high doping, $\sigma_{xx}^{(D)}$ and $\sigma_{yy}^{(D)}$ continues to increase with the Fermi energy. The increasing nature of Drude conductivities with the Fermi energy can be explained by the monotonous increase of Fermi surface area and velocities with μ for given δ_0 . It is to be noted that for high Fermi energy, the Fermi surface topology relatively remains the same with δ_0 .

We also note the variation for the geometric mean of Drude conductivities defined as $\sigma_P = \sqrt{\sigma_{xx}^{(D)} \sigma_{yy}^{(D)}}$ and their ratio $\sigma_R \equiv \sigma_{xx}^{(D)}/\sigma_{yy}^{(D)}$ with μ and δ_0 . We are interested in probing the variations of experimentally relevant quantity σ_R which is independent of scattering time since the calculation of scattering time may not be straightforward. We find that σ_P is independent of α and β . Similar to Drude conductivities, σ_P also shows an increase with the Fermi energy. However, the ratio σ_R decreases with Fermi energy for low doping while for high doping, it shows an increase with the Fermi energy for a given δ_0 . Note that for low doping, the semi-Dirac curve ($\delta_0 = 0$) for σ_R deviates significantly from the finite δ_0 case. For

$\delta_0 = 0$, σ_R increases with the Fermi energy whereas decreases for finite δ_0 . For high doping, the resulting ratio curve matches perfectly well with the semi-Dirac case. Next, we discuss the variation of these quantities as a function of δ_0 for a given Fermi energy. We find that for low doping, σ_P is nearly constant which is consistent with our results of $\gamma \rightarrow \infty$ limit, while for high doping, σ_P shows an increase with δ_0 . The ratio σ_R increases with δ_0 . This variation for the geometric mean and ratio of Drude conductivities are illustrated in Figs. 5(a) and 5(b) respectively.

Now we move to compute the magnetic field-dependent linear conductivities of the system. The Lorentz force-induced Hall conductivity can be calculated using Eq. (A6) as

$$\begin{aligned} \sigma_{xy}^{(L)} &= -\frac{\sqrt{2}\sigma_0 \tilde{B}_1}{15\pi^2} \frac{\tilde{\delta}_0^{5/2}}{\sqrt{\gamma(\tilde{\delta}_0^2 + \tilde{m}_0^2\gamma^2)}} \\ &\begin{cases} [(2\gamma^2 + 7\gamma - 9)K(k) + 2(9 - 2\gamma^2)E(k)], & \gamma < 1, \\ 2k[(9 - 2\gamma^2)E(k') + 2\gamma(\gamma - 1)K(k')], & \gamma \geq 1. \end{cases} \end{aligned} \quad (24)$$

Here, $\sigma_{xy}^{(L)} = -\sigma_{yx}^{(L)}$ and $\tilde{B}_1 = B/B_1$ with $B_1 = \hbar^2/(e\tau\alpha)$. Expanding the low-energy expression up to the leading order in k' , we find

$$\sigma_{xy}^{(L)} \simeq \frac{-\sigma_0 \tilde{B}_1}{16\pi} \frac{\tilde{\delta}_0^{5/2}}{\sqrt{\gamma(\tilde{\delta}_0^2 + \tilde{m}_0^2\gamma^2)}} \left[\frac{(1+2\gamma)(3+4\gamma)}{(\gamma+1)^{3/2}} \right]. \quad (25)$$

In the limit of $\gamma \rightarrow \infty$, it turns out that $\sigma_{xy}^{(L)} \propto (\mu^2)\sqrt{\delta_0}$. The variation of $\sigma_{xy}^{(L)}$ with the Fermi energy is shown in Fig. 4(c). Below the saddle point for $\gamma > 1$, $\sigma_{xy}^{(L)}$ increases with the increase in Fermi energy and δ_0 . In other words, $\sigma_{xy}^{(L)}$ decreases as Dirac nodes moves closer to each other ($\delta_0 \rightarrow 0$). As expected, a little kink is observed at the saddle point. Past the saddle point, $\sigma_{xy}^{(L)}$ continues to monotonically increasing with μ . For high Fermi energy, $\sigma_{xy}^{(L)}$ increases with δ_0 . The OMM induced Hall conductivity can be evaluated using Eq. (A7) as

$$\begin{aligned} \sigma_{xy}^{(OMM)} = -\sigma_{yx}^{(OMM)} &= -\frac{\sigma_0 \tilde{m}_0^2 \tilde{B}_2}{2\sqrt{2}\pi^2} \frac{\sqrt{\gamma^7 \tilde{\delta}_0}}{(\tilde{\delta}_0^2 + \tilde{m}_0^2\gamma^2)^2} \\ &\begin{cases} [2E(k) - (1-\gamma)K(k)], & \gamma < 1, \\ 2k[E(k')], & \gamma \geq 1, \end{cases} \end{aligned} \quad (26)$$

where $\tilde{B}_2 = B/B_2$ with $B_2 = \tau\hbar^4\beta^4/(e\alpha^3)$. Expanding the above expression for $\gamma \geq 1$, we find

$$\sigma_{xy}^{(OMM)} \simeq \frac{\sigma_0 \tilde{m}_0^2 \tilde{B}_2}{64\pi} \frac{\sqrt{\gamma^7 \tilde{\delta}_0}}{(\tilde{\delta}_0^2 + \tilde{m}_0^2\gamma^2)^2} \left[\frac{(1+4\gamma)(5+4\gamma)}{(\gamma+1)^{3/2}} \right]. \quad (27)$$

We find that the $\sigma_{xy}^{(OMM)}$ varies as $\sqrt{\delta_0}$ in $\gamma \rightarrow \infty$ limit. For low doping, $\sigma_{xy}^{(OMM)}$ decreases with the Fermi energy whereas increases with δ_0 . Above the saddle point, it continues to decrease with μ while increases with δ_0 .

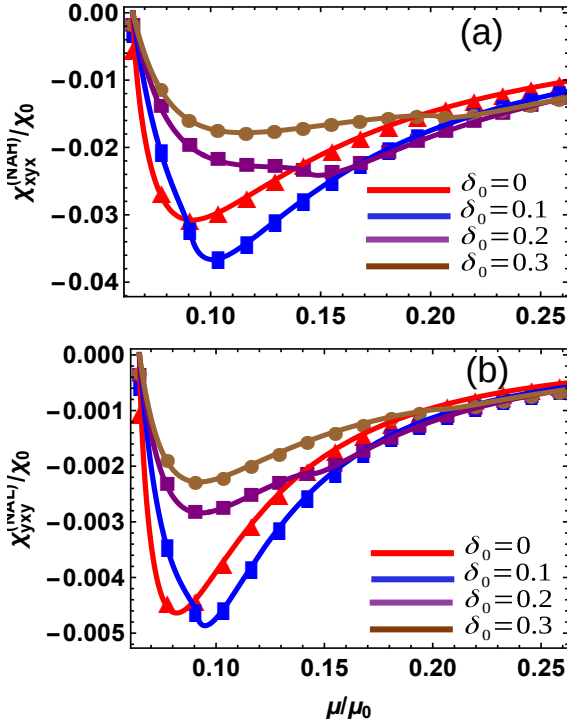


FIG. 6: (a) Depicts the behavior of SH anomalous Hall conductivity with the Fermi energy. (b) The anomalous velocity and Lorentz force induced SH conductivity as a function of Fermi energy. Both of these plots are plotted for different values of δ_0 in eV. The solid color curves are the results of analytical calculations at zero temperature which matches perfectly well with the numerical results obtained at $T = 34$ K (color plot markers). The above SH conductivities are normalized by $\chi_0 = e^3 \tau \alpha / \hbar^3 \beta$. The parameters used are the same as in Fig. 4.

Note that this energy dependence of $\sigma_{xy}^{(OMM)}$ is related to the fact that the magnitude of Berry curvature and OMM decreases as the Fermi energy shifts away from the band edge. It is evident from Fig. 4(d) that the magnitude of OMM induced Hall conductivity is considerably smaller than the other linear contributions.

We would like to point out that the linear conductivities $\sigma_{xx}^{(D)}$, $\sigma_{xy}^{(L)}$ and $\sigma_{xy}^{(OMM)}$ are predicted to be large for materials with small effective mass, whereas $\sigma_{yy}^{(D)}$ appears small for low effective mass. The effective mass of some proposed semi-Dirac materials are $m^* = 13.6m_e$ for $(\text{TiO}_2)_5/(\text{VO}_2)_3$, $m^* = 3.1m_e$ (α -(BEDT-TTF) $_2\text{I}_3$) and $m^* = 1.2 * 10^{-3}m_e$ (photonic crystals)⁵⁹. We have used $m^* = 13.6m_e$, $\beta = 10^5$ m/s, $m_0 = 0.1$ eV, $\alpha = 2.7$ meV.nm², $B = 2$ T and $\tau = 10^{-12}$ s in this work. We also find that the linear conductivities decrease with the increase of gap parameter m_0 at a given value of μ and δ_0 . It is to be noted that only the Hall components of the above B -linear contribution to the conductivity survive due to the Onsager relation which implies $\sigma_{ij}(B) = \sigma_{ji}(-B)$. We have also calculated these contributions to the linear conductivities numerically at $T = 34$

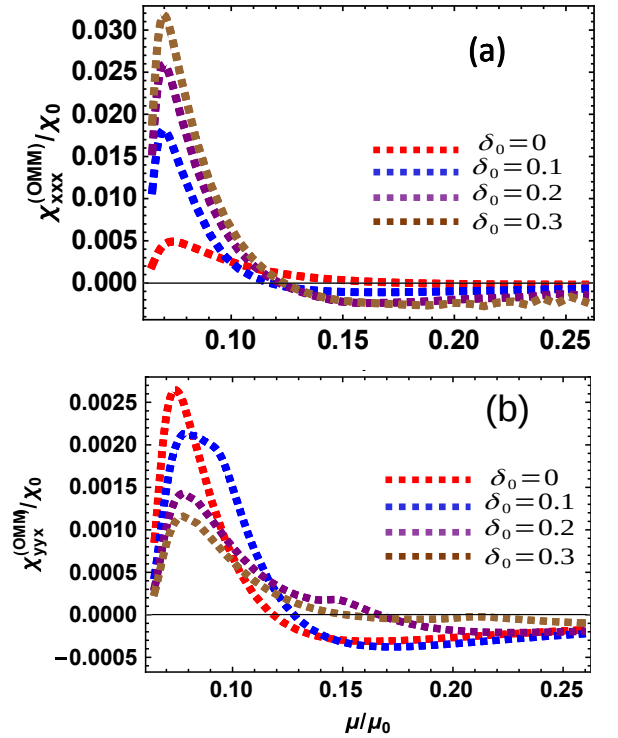


FIG. 7: (a)-(b) OMM induced SH conductivity as a function of Fermi energy for different values of δ_0 in eV. The dashed color curves denote the results calculated numerically at $T = 34$ K. The parameters used are the same as in Fig. 4.

K and the obtained results at $T = 34$ K match well with the analytical results evaluated at zero temperature.

Nonlinear conductivities

A. Second-harmonic conductivities

Next, we calculate the different contributions (arising from Berry curvature and OMM) to the SH conductivities of the system. Following the details of calculation similar to the linear case related to the integration over energy and ϕ in two regimes, the SH anomalous Hall conductivity can be evaluated using Eq. (7) as

$$\chi_{xyx}^{(NAH)} = -\frac{\chi_0 \tilde{m}_0}{6\sqrt{2}\pi^2} \frac{(\gamma \tilde{\delta}_0)^{3/2}}{(\tilde{\delta}_0^2 + \tilde{m}_0^2 \gamma^2)^{3/2}} \begin{cases} [(1-\gamma)K(k) + 2\gamma E(k)], & \gamma < 1, \\ 2k[(1-\gamma)K(k') + \gamma E(k')], & \gamma \geq 1, \end{cases} \quad (28)$$

where $\chi_0 = e^3 \tau \alpha / \hbar^3 \beta$. The other nonvanishing components of SH anomalous conductivity goes as $\chi_{yxx}^{(NAH)} = -\chi_{xyx}^{(NAH)}$. These off-diagonal terms are proportional to the x -component of the Berry curvature dipole which is nonzero due to the mirror symmetry along the x axis⁵⁹.

We obtained the SH Hall conductivity arising due to the effective combination of Lorentz force and anomalous

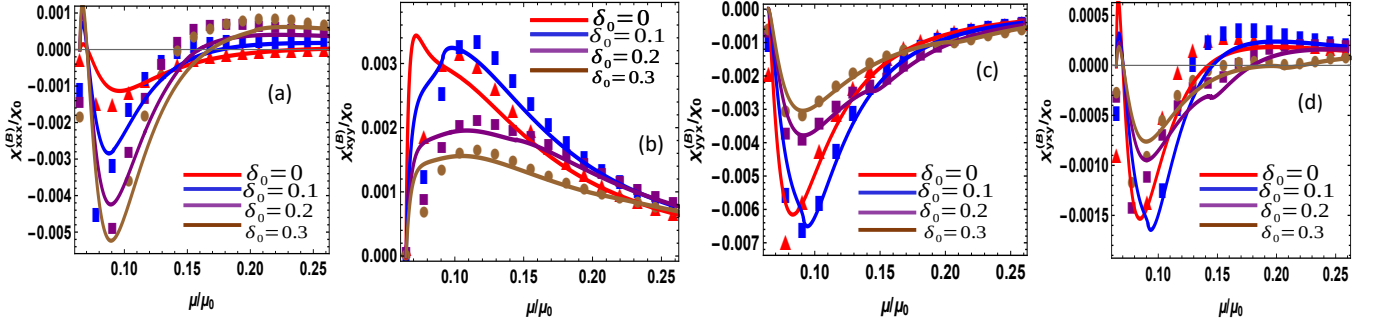


FIG. 8: (a)-(d) Variation of different components of phase-space factor induced SH conductivity (measured in units of χ_0) with the Fermi energy for different values of δ_0 in eV. The solid color curves are the results calculated at zero temperature, while color plot markers represent the numerical results obtained at $T = 34$ K. The parameters used are the same as in Fig. 4.

$j \propto E^n$	$B=0$		$B \neq 0$		
	Drude	Anomalous Hall	Lorentz force and anomalous velocity	phase-space factor (B)	Orbital Magnetic moment (OMM)
$n = 1$ linear current responses	$\sigma_{xx}^{(D)} \neq \sigma_{yy}^{(D)}$	0	$\sigma_{xy}^{(L)} = -\sigma_{yx}^{(L)}$	0	$\sigma_{xy}^{(OMM)} = -\sigma_{yx}^{(OMM)}$
$n = 2$ SH current responses	0	$\chi_{yxx}^{(NAH)} = -\chi_{xyx}^{(NAH)}$	$\chi_{xyy}^{(NAL)} = -\chi_{yyx}^{(NAL)}$	$\chi_{xxx}^{(B)}, \chi_{xyy}^{(B)}, \chi_{yyx}^{(B)}, \chi_{yxx}^{(B)}$	$\chi_{xxx}^{(OMM)}, \chi_{xyy}^{(OMM)} = \chi_{yxx}^{(OMM)}, \chi_{yyx}^{(OMM)}$

TABLE I: Highlighting the nonzero components of different contributions induced by the Berry curvature and the OMM to the linear and SH conductivities (up to linear order in a magnetic field).

velocity for the system using Eq. (9) and find it is related to SH anomalous Hall conductivity as

$$\chi_{yxy}^{(NAL)} = \frac{\tilde{B}_1}{\mu/\mu_0} \chi_{xyx}^{(NAH)}. \quad (29)$$

The other nonzero Hall component is $\chi_{xyy}^{(NAL)} = -\chi_{yyx}^{(NAL)}$. It is evident from the above equation that the ratio $\chi_{yxy}^{(NAL)}/\chi_{xyx}^{(NAH)}$ is independent of δ_0 . For the parameters used in our calculation and $\mu = 0.2$ eV, we get $\tilde{B}_1\mu_0/\mu = 0.1$. Hence, $\chi_{yxy}^{(NAL)}$ is about an order of magnitude less than $\chi_{xyx}^{(NAH)}$. Thus, the intrinsic anomalous response dominates over the Lorentz force contribution. Expanding the exact analytical results given by Eqs. (28) and (29) for $\gamma \geq 1$, we obtain

$$\chi_{xyx}^{(NAH)} \simeq \frac{-\chi_0 \tilde{m}_0}{64\pi} \frac{(\gamma \tilde{\delta}_0)^{3/2}}{(\tilde{\delta}_0^2 + \tilde{m}_0^2 \gamma^2)^{3/2}} \left[\frac{4\gamma + 11}{(1 + \gamma)^{3/2}} \right]. \quad (30)$$

$$\chi_{yxy}^{(NAL)} \simeq \frac{\tilde{B}_1 \gamma}{\sqrt{\tilde{\delta}_0^2 + \tilde{m}_0^2 \gamma^2}} \chi_{xyx}^{(NAH)}.$$

Near the band-edge at $\gamma \rightarrow \infty$, we find that $\chi_{xyx}^{(NAH)}$ and $\chi_{yxy}^{(NAL)} \propto \mu^2/\sqrt{\delta_0}$. For low doping, both the SH conductivities increase with μ but decrease with δ_0 . As Fermi energy is further increased, both $\chi_{xyx}^{(NAH)}$ and $\chi_{yxy}^{(NAL)}$ start decreasing with μ , although a substantial change is not observed with δ_0 in the region of high Fermi energy. A small kink is observed at the saddle point which reflects

the change in Fermi surface topology. The Fermi energy dependence of $\chi_{xyx}^{(NAH)}$ and $\chi_{yxy}^{(NAL)}$ for different values of δ_0 is depicted in Figs. 6(a) and 6(b) respectively. The peaks in $\chi_{yxy}^{(NAL)}$ appear to be more pronounced than the peaks seen in $\chi_{xyx}^{(NAH)}$.

We next turn to evaluate the OMM contribution to the SH conductivity using Eq. (10). We start by performing the integral over energy analytically using the approximation $f'_{\text{eq}} = -\delta(\epsilon_{\mathbf{k}} - \mu)$ in the limit of $T \rightarrow 0$, where we find that the resulting expression encounters divergence, unlike the previous cases. Thus the zero temperature approximation of the Dirac-delta function does not capture the proper results here. Therefore we proceed to calculate the OMM contribution by computing the results numerically at finite temperature $T = 34$ K to overcome the issue of divergence. Figure 7 represents the variation of OMM induced SH conductivities ($\chi_{xxx}^{(OMM)}$ and $\chi_{yxy}^{(OMM)} = \chi_{xyy}^{(OMM)} = \chi_{yyx}^{(OMM)}$) with the Fermi energy.

The phase-space contribution to the SH conductivity can be calculated using Eq. (11). Its expression after integration over energy (at zero temperature) is cumbersome and therefore not presented over here. The nonzero components of phase-space induced conductivity includes diagonal term $\chi_{xxx}^{(B)}$ and off-diagonal components $\chi_{yxy}^{(B)}$, $\chi_{xyy}^{(B)}$ and $\sigma_{xyy}^{(B)}$. We have plotted the Fermi energy dependence of these terms for different values of δ_0 in Fig. 8. Similar to the linear case, we have plotted the above three contributions to the SH conductivity by performing numerical calculations at temperature $T = 34$ K and

we observed that they agree closely with our analytical results obtained at zero temperature. Both the SH conductivities, $\chi_{abc}^{(\text{OMM})}$ and $\chi_{abc}^{(\text{B})}$ initially show an increase with the Fermi energy but then start decreasing.

We emphasize that all the above SH conductivities have a peak near the band edge which is related to the fact that these SH contributions arise from the Berry curvature and OMM and their magnitude decreases as the Fermi energy shifts from the band edge. The peaks are not observed exactly at the band edge because the SH contributions arise from the effective contribution of geometric quantities and band dispersion anisotropy. The nonzero components of these different contributions are highlighted in Table I. It is worth pointing out that all four contributions to the SH conductivities increase with

the decrease in the effective band mass of semi-Dirac materials. Interestingly, these SH conductivities in a given semi-Dirac material are found to be comparable or order smaller than the SH conductivities of a 2D system hosting massive tilted Dirac fermions⁶⁸. We also noticed the variation of SH conductivities with the gap parameter m_0 and find that their peak is shifted with the increase of m_0 .

B. Nonlinear DC current

We next proceed to calculate the NL dc current arising from these different contributions in the gapped semi-Dirac system using Eqs. (12) and (B1)-(B3),

$$\mathbf{j}_{\text{NAH}}^{(0)} = \frac{\chi_{xyx,0}^{(\text{NAH})}}{1 + \omega^2\tau^2} \left[-2|E_x|^2\hat{\mathbf{y}} + [E_y E_x^*]_+\hat{\mathbf{x}} - i\omega\tau[E_y E_x^*]_-\hat{\mathbf{x}} \right], \quad (31)$$

$$\mathbf{j}_{\text{NAL}}^{(0)} = \frac{\chi_{xyx,0}^{(\text{NAL})}}{(1 + \omega^2\tau^2)^2} \left[(1 - \omega^2\tau^2) \left(-2|E_y|^2\hat{\mathbf{x}} + [E_y E_x^*]_+\hat{\mathbf{y}} \right) + 2i\omega\tau[E_y E_x^*]_-\hat{\mathbf{y}} \right], \quad (32)$$

$$\mathbf{j}_{\text{OMM}}^{(0)} = \frac{2}{1 + \omega^2\tau^2} \left[\chi_{xxx,0}^{(\text{OMM})}|E_x|^2\hat{\mathbf{x}} + \chi_{yyx,0}^{(\text{OMM})} \left(|E_y|^2\hat{\mathbf{x}} + [E_y E_x^*]_+\hat{\mathbf{y}} \right) \right], \quad (33)$$

$$\mathbf{j}_{\text{B}}^{(0)} = \frac{1}{1 + \omega^2\tau^2} \left[2 \left(\chi_{xxx,0}^{(\text{B})}|E_x|^2 + \chi_{xyy,0}^{(\text{B})}|E_y|^2 \right) \hat{\mathbf{x}} + \left(\chi_{yyx,0}^{(\text{B})} + \chi_{xyx,0}^{(\text{B})} \right) [E_y E_x^*]_+\hat{\mathbf{y}} - i\omega\tau \left(\chi_{yyx,0}^{(\text{B})} - \chi_{xyx,0}^{(\text{B})} \right) [E_y E_x^*]_-\hat{\mathbf{y}} \right]. \quad (34)$$

It is evident that the obtained NL dc current is dependent on the polarization of the incident electromagnetic wave. Here, we define the total NL dc current as $\mathbf{j}_{\text{net}}^{(0)} = j_x^{(0)}\hat{\mathbf{x}} + j_y^{(0)}\hat{\mathbf{y}} = \mathbf{j}_{\text{NAH}}^{(0)} + \mathbf{j}_{\text{NAL}}^{(0)} + \mathbf{j}_{\text{OMM}}^{(0)} + \mathbf{j}_{\text{B}}^{(0)}$ and discuss their contributions in response to the linearly and circularly polarized light.

Case I: For linearly polarized light in the x direction, i.e., $\mathbf{E} = (E_0, 0, 0)$, the total NL dc current along the x and y direction can be calculated as

$$\begin{aligned} j_x^{(0)} &= \frac{2}{1 + \omega^2\tau^2} (\chi_{xxx,0}^{(\text{OMM})} + \chi_{xxx,0}^{(\text{B})}) |E_0|^2, \\ j_y^{(0)} &= -\frac{2}{1 + \omega^2\tau^2} \chi_{xyx,0}^{(\text{NAH})} |E_0|^2. \end{aligned} \quad (35)$$

In the low-frequency limit $\omega\tau \ll 1$, the above equation reduces to $j_x^{(0)} \approx 2(\chi_{xxx,0}^{(\text{OMM})} + \chi_{xxx,0}^{(\text{B})}) |E_0|^2$ and $j_y^{(0)} \approx -2\chi_{xyx,0}^{(\text{NAH})} |E_0|^2$. We have plotted the variation of $j_x^{(0)}$ and $j_y^{(0)}$ with the Fermi energy for $\delta_0 = 0.1$ eV in inset of Fig. 9(a). For very low Fermi energy below the saddle point, $j_x^{(0)}$ and $j_y^{(0)}$ are comparable and thus the angle which the total DC current $\mathbf{j}_{\text{net}}^{(0)}$ makes with the x axis (say, θ) increases monotonically with the Fermi energy. For high Fermi energy above the saddle point, $j_x^{(0)}$ becomes vanishingly small and nearly constant as

compared to $j_y^{(0)}$. Thus $j_y^{(0)}$ dominates and the angle between the $\mathbf{j}_{\text{net}}^{(0)}$ and x axis saturates, $\theta \rightarrow 90^\circ$ implying that the total dc current is nearly perpendicular to the applied electric field as shown in Fig. 9(a). This can be attributed to the fact that $j_y^{(0)} \propto \chi_{xyx,0}^{(\text{NAH})}$, which is finite due to the x component of Berry curvature dipole. This Berry curvature dipole contribution arises from the mirror symmetry along the x axis in the system. However, in the absence of B , the NL dc current is purely along the y -direction for any Fermi energy. In the high frequency limit $\omega\tau \gg 1$, $j_x^{(0)}$ and $j_y^{(0)}$ are simply reduced by a factor of $\omega^2\tau^2$.

Case II: For linearly polarized light in the y direction, i.e., $\mathbf{E} = (0, E_0, 0)$, the NL dc current contribution in the x and y direction can be obtained as

$$\begin{aligned} j_x^{(0)} &= \frac{2}{1 + \omega^2\tau^2} \left[-\left(\frac{1 - \omega^2\tau^2}{1 + \omega^2\tau^2} \right) \chi_{xyx,0}^{(\text{NAL})} + \chi_{yyx,0}^{(\text{OMM})} \right. \\ &\quad \left. + \chi_{xyy,0}^{(\text{B})} \right] |E_0|^2, \\ j_y^{(0)} &= 0. \end{aligned} \quad (36)$$

In the $\omega\tau \ll 1$ limit, we obtain $j_x^{(0)} \approx 2(-\chi_{xyx,0}^{(\text{NAL})} + \chi_{yyx,0}^{(\text{OMM})} + \chi_{xyy,0}^{(\text{B})}) |E_0|^2$ and $j_y^{(0)} = 0$ which indicates the

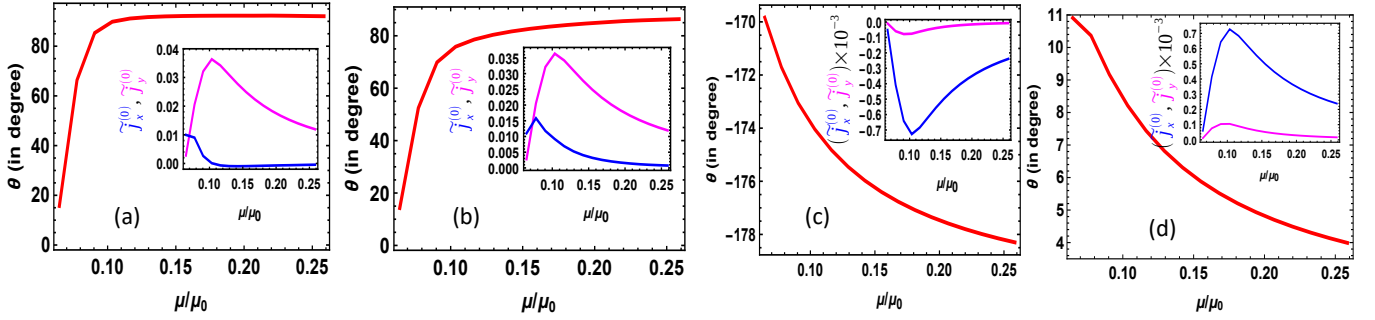


FIG. 9: Variation of angle between the total NL dc current $\mathbf{j}_{\text{net}}^{(0)}$ and the x axis (defined as θ) with the Fermi energy at $\delta_0 = 0.1$ eV for: (a) linearly polarized light along the x direction, (b) left and right circularly polarized light in the limit of $\omega\tau \ll 1$, (c)-(d) left and right circularly polarized light in the $\omega\tau \gg 1$ limit. The corresponding insets represent the Fermi energy dependence of the total NL dc current in the x and y directions denoted by $j_x^{(0)}$ and $j_y^{(0)}$ respectively. We have defined the scaled dc current as $\tilde{j}_x^{(0)} = j_x^{(0)}/(2\chi_0|E_0|^2)$ and $\tilde{j}_y^{(0)} = j_y^{(0)}/(2\chi_0|E_0|^2)$. The other parameters used are the same as in Fig. 4.

direction of $\mathbf{j}_{\text{net}}^{(0)}$ is directed along the positive x direction, i.e., $\theta = 0$. When $\omega\tau \gg 1$, the current in the x direction is given by $j_x^{(0)} \approx (2/\omega^2\tau^2)(\chi_{yxy,0}^{(\text{NAL})} + \chi_{yyx,0}^{(\text{OMM})} + \chi_{xyy,0}^{(\text{B})})|E_0|^2$. The values of $j_x^{(0)}$ becomes negative due to which $\mathbf{j}_{\text{net}}^{(0)}$ is oriented antiparallel to the x axis, i.e., $\theta = 180^\circ$. These currents vanish in the absence of a magnetic field.

Case III: For circularly polarized light, the electric field is given by $\mathbf{E} = (E_0, \Lambda iE_0, 0)$, where the index $\Lambda = \pm$ indicates left and right circularly polarized light, respectively. The total NL dc current in the x and y direction can be obtained as

$$j_x^{(0)} = \frac{2}{1 + \omega^2\tau^2} \left[\Lambda\omega\tau\chi_{xyx,0}^{(\text{NAH})} - \left(\frac{1 - \omega^2\tau^2}{1 + \omega^2\tau^2} \right) \chi_{yxy,0}^{(\text{NAL})} + \chi_{xxx,0}^{(\text{OMM})} + \chi_{yyx,0}^{(\text{OMM})} + \chi_{xxx,0}^{(\text{B})} + \chi_{xyy,0}^{(\text{B})} \right] |E_0|^2, \quad (37)$$

$$j_y^{(0)} = \frac{2}{1 + \omega^2\tau^2} \left[-\chi_{xyx,0}^{(\text{NAH})} - \Lambda \left(\frac{2\omega\tau}{1 + \omega^2\tau^2} \right) \chi_{yxy,0}^{(\text{NAL})} + \Lambda\omega\tau(\chi_{yyx,0}^{(\text{B})} - \chi_{xyy,0}^{(\text{B})}) \right] |E_0|^2.$$

(a). In the $\omega\tau \ll 1$ limit: The terms in the above equation with the coefficient $\omega\tau$ correspond to the CPGE. Note that the CPGE vanishes in this limit, which implies that there is no difference between the effects of left and right circularly polarized light. For low Fermi energy, $j_x^{(0)}$ and $j_y^{(0)}$ are comparable due to which the angle between $\mathbf{j}_{\text{net}}^{(0)}$ and the x axis increases with the Fermi energy. In the high Fermi energy region, both $j_x^{(0)}$ and $j_y^{(0)}$ decrease with the Fermi energy. However, the major contribution to the $\mathbf{j}_{\text{net}}^{(0)}$ comes from $j_y^{(0)} \propto \chi_{xyx,0}^{(\text{NAH})}$. Hence, θ shows a gradual increase with the Fermi energy, approaching the value close to 90° (pointing in the direction close to the y axis) as shown in Fig. 9(b). In the absence of B , the NL dc current is purely along the y -direction for any Fermi energy.

(b). In the $\omega\tau \gg 1$ limit: The NL dc current in the x and y direction yields the form, $j_x^{(0)} \propto (1/\omega\tau)\chi_{xyx,0}^{(\text{NAH})}$ and $j_y^{(0)} \propto (1/\omega\tau)(\chi_{yyx,0}^{(\text{B})} - \chi_{xyy,0}^{(\text{B})})$, respectively. Interestingly, we find that the current $j_x^{(0)}$ approaches the intrinsic value i.e., independent of scattering time τ . The

dominant contribution comes from $j_x^{(0)} \propto \chi_{xyx,0}^{(\text{NAH})}$. For left circularly polarized light, the current $\mathbf{j}_{\text{net}}^{(0)}$ flows nearly antiparallel to the x axis, $\theta \rightarrow -180^\circ$ [Fig. 9(c)]. The NL dc current points exactly along the negative x -direction in the absence of B . While for right circularly polarized light, $\mathbf{j}_{\text{net}}^{(0)}$ flows in a direction almost parallel to the x axis with $\theta \rightarrow 0$ [Fig. 9(d)]. The NL dc current is directed purely along the positive x -direction without B , for any Fermi energy.

Therefore, we conclude that the direction of the NL DC current depends on the Fermi energy, magnetic field and the polarization of the electromagnetic wave. It is predominantly governed by the underlying mirror symmetry of the system.

V. SECOND-ORDER NONLINEAR VOLTAGE RESPONSES

In the previous section, we have studied the linear, SH and NL dc current responses of the semi-Dirac system

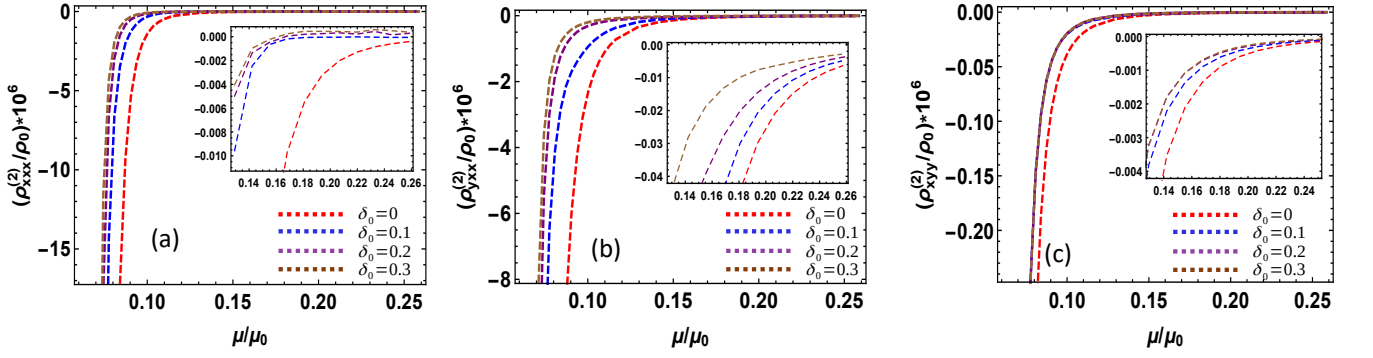


FIG. 10: (a) SH resistivity $\rho_{xx}^{(2)}$ and (b) SH Hall resistivity $\rho_{yxx}^{(2)}$ as a function of Fermi energy for different values of δ_0 (when current is applied along the x -direction). (c) The variation of SH Hall resistivity $\rho_{xyy}^{(2)}$ with the Fermi energy (when current is applied along the y -direction). The insets represent the blow-up of the region where Fermi energy μ ranges from 0.2 eV to 0.4 eV. The normalization parameter for SH resistivity is defined as $\rho_0 = \alpha^4 / (e^3 \hbar^3 \tau^2 \beta^7)$. The dashed color curves represent the numerical results obtained at $T = 34$ K. The parameters used are the same as in Fig. 4.

(through the conductivity tensors) on application of an oscillating electric field and a weak magnetic field. In this section, we look at the inverse process i.e. the induction of linear, SH and NL dc voltage/electric fields on passing an ac current through the system^{50,68–70}. Here, ‘NL’ would imply the order of applied current. These induced electric fields are related to the applied ac current j^ω by introducing resistivity into the picture. The linear resistivity ρ_{ab} is defined as $E_a^\omega = \rho_{ab} j_b^\omega$, whereas the SH resistivity $\rho_{abc}^{(2\omega)}$ is given by $E_a^{2\omega} = \rho_{abc}^{(2\omega)} j_b^\omega j_c^\omega$ and the NL DC resistivity goes as $E_a^{\text{nl-dc}} = \rho_{abc}^{\text{nl-dc}} j_b^{\text{dc}} j_c^{\text{dc}}$.

A. Linear resistivity

The linear resistivity matrix can be simply obtained by inverting the linear conductivity matrix. Keeping the lowest order magnetic field dependence, the linear resistivities can be calculated using $\rho_{xx} = 1/\sigma_{xx}^{(D)}$, $\rho_{xy} = -\rho_{yx} = -\sigma_{xy}^{(L)} / (\sigma_{xx}^{(D)} \sigma_{yy}^{(D)})$ and $\rho_{yy} = 1/\sigma_{yy}^{(D)}$. Note that we have ignored the OMM induced Hall conductivity contribution as its magnitude is much small as compared to Lorentz force induced Hall conductivity, $\sigma_{xy}^{(\text{OMM})} \ll \sigma_{xy}^{(L)}$. We find that the linear longitudinal resistivity, $\rho_{xx} \propto B^0$ and linear Hall resistivity, $\rho_{xy} \propto B$. These linear resistivities show a decrease with Fermi energy.

B. Nonlinear resistivity

Unlike the linear resistivity case, the NL resistivity matrix cannot be obtained directly by inverting the NL conductivity matrix. Instead, the second-order NL resistivity is defined in terms of second-order NL conductivities and linear resistivities⁶⁸ as

$$\rho_{abc}^{(2)} = -\rho_{ai} \chi_{ijk} \rho_{jb} \rho_{kc}. \quad (38)$$

Note that Eq. (38) remains valid for both the SH resistivity and the NL dc resistivity, depending on which NL conductivity is employed on the right-hand side. Here, we present the results for the SH resistivity in the transport limit, $\omega\tau \ll 1$, obtained by applying the current along the x and y directions. It is worth pointing out that, in this limit, the SH resistivities are nearly equal to the NL dc resistivities.

Case I. Current applied along the x -direction:

We consider that the current is flowing only along the x -direction, then the components of the SH resistivity matrix for 2D systems can be written as

$$\begin{pmatrix} \rho_{xxx}^{(2)} \\ \rho_{yxx}^{(2)} \end{pmatrix} = -[\rho] \begin{pmatrix} \chi_{xxx} & \chi_{xxy} & \chi_{xyx} & \chi_{xyy} \\ \chi_{yxx} & \chi_{yyx} & \chi_{yyx} & \chi_{yyy} \end{pmatrix} \begin{pmatrix} \rho_{xx}^2 \\ \rho_{xx}\rho_{yx} \\ \rho_{xx}\rho_{yx} \\ \rho_{yy}^2 \end{pmatrix}. \quad (39)$$

Here, $\rho_{xxx}^{(2)}$ and $\rho_{yxx}^{(2)}$ denote the SH longitudinal and SH Hall resistivities respectively and $[\rho]$ is the 2×2 linear resistivity matrix. We further simplify the above equation by keeping the lowest-order magnetic field dependence and ignoring the quadratic and higher B -field dependent terms lead to

$$\begin{aligned} \rho_{xxx}^{(2)} &= -\rho_{xx}^2 (\chi_{xxx}\rho_{xx} + \chi_{xyx}\rho_{yx} + \chi_{yxx}\rho_{xy}), \\ \rho_{yxx}^{(2)} &= -\rho_{xx}^2 \chi_{yxx}\rho_{yy}. \end{aligned} \quad (40)$$

We find that the lowest-order magnetic field dependence of these SH resistivities goes as $\rho_{xxx}^{(2)} \propto B$ and $\rho_{yxx}^{(2)} \propto B^0$ which is distinct from the linear resistivities. It is evident from Eq. (40) that $\rho_{xxx}^{(2)}$ depend on SH conductivities and linear Hall resistivities. Note that longitudinal resistivity $\rho_{xxx}^{(2)}$ in the absence of magnetic field becomes zero as $\chi_{xxx}(B=0)=0$. Thus we emphasize that the predicted B -linear dependence of $\rho_{xxx}^{(2)}$ arises mainly from the diagonal component of SH conductivity ($\chi_{xxx} = \chi_{xxx}^{(\text{OMM})} + \chi_{xxx}^{(B)}$) which remains finite due to

$E \propto j^n$	$B=0$	$B \neq 0$
$n=1$ linear voltage responses $E_a^\omega = \rho_{ab} j_b^\omega$	ρ_{xx}, ρ_{yy}	$\rho_{xy} = -\rho_{yx}$
$n=2$ SH voltage responses $E_a^{2\omega} = \rho_{abb}^{(2\omega)} (j_b^\omega)^2$	$\rho_{yxx}^{(2)}$	$\rho_{xxx}^{(2)}, \rho_{xyy}^{(2)}$

TABLE II: Highlighting the nonzero components of linear and SH resistivities up to linear order in a magnetic field.

the surviving mirror symmetry along the x -direction. The NL resistivities originate from Berry curvature and OMM and therefore has a quantum mechanical origin. The SH resistivities $\rho_{xxx}^{(2)}$ and $\rho_{yxx}^{(2)}$ show a relatively significant decrease with the Fermi energy for low doping as compared to high doping which is illustrated in Figs. 10(a) and 10(b). Furthermore, the scattering time dependence of SH resistivities is found to be $\rho_{xxx}^{(2)} \propto 1/\tau$ and $\rho_{yxx}^{(2)} \propto 1/\tau^2$. Thus, the experimentally connected scattering time independent ratios are defined for SH resistivities as $\rho_{xxx}^{(2)}/\rho_{xx}$ and $\rho_{yxx}^{(2)}/\rho_{xx}^2$. We find that $\rho_{xxx}^{(2)}/\rho_{xx}$ (\sim ratio of SH longitudinal voltage to the product of linear voltage and current) decreases with the Fermi energy and δ_0 whereas $\rho_{yxx}^{(2)}/\rho_{xx}^2$ (\sim ratio of SH Hall voltage to the square of linear voltage) decreases with Fermi energy but independent of δ_0 . Unlike the linear and SH conductivities, the change in Fermi surface topology is not reflected in the SH resistivities through the kink.

Case II. Current applied along the y -direction:

In the wake of anisotropic energy dispersion, the current is also applied along the y -direction and the corresponding SH resistivity matrix turns out to be

$$\begin{pmatrix} \rho_{xyy}^{(2)} \\ \rho_{yyy}^{(2)} \end{pmatrix} = -[\rho] \begin{pmatrix} \chi_{xxx} & \chi_{xxy} & \chi_{xyx} & \chi_{xyy} \\ \chi_{yxx} & \chi_{yyx} & \chi_{yyx} & \chi_{yyy} \end{pmatrix} \begin{pmatrix} \rho_{xy}^2 \\ \rho_{xy}\rho_{yy} \\ \rho_{xy}\rho_{yy} \\ \rho_{yy}^2 \end{pmatrix}. \quad (41)$$

Focusing on the lowest-order magnetic field dependence terms, we get

$$\begin{aligned} \rho_{yyy}^{(2)} &= 0, \\ \rho_{xyy}^{(2)} &= -\rho_{xx}\rho_{yy}(\chi_{xyx}\rho_{xy} + \chi_{xyy}\rho_{yy}). \end{aligned} \quad (42)$$

Here, the SH longitudinal resistivity $\rho_{yyy}^{(2)}$ vanishes and the SH Hall resistivity $\rho_{xyy}^{(2)} \propto B$. The SH Hall resistivity $\rho_{xyy}^{(2)}$ in the absence of magnetic field comes zero as $\chi_{xyy}(B=0) = 0$. Hence this B -linear dependence of $\rho_{xyy}^{(2)}$ originally arises from the SH Hall conductivity ($\chi_{xyy} = \chi_{xyy}^{(\text{NAL})} + \chi_{xyy}^{(\text{OMM})} + \chi_{xyy}^{(\text{B})}$) which elucidates that $\rho_{xyy}^{(2)}$ also depends on intrinsic band geometric quantities.

The SH Hall resistivity $\rho_{xyy}^{(2)}$ decreases with the Fermi energy as shown in Fig. 10(c). The scattering time dependence goes as $\rho_{xyy}^{(2)} \propto 1/\tau$ and the ratio $\rho_{xyy}^{(2)}/\rho_{yy} \propto \tau^0$. We notice that the ratio $\rho_{xyy}^{(2)}/\rho_{yy}$ decreases with the Fermi energy and δ_0 . The nonzero components of resistivities are summarized in Table II.

Some key observations about the SH resistivities of this system are as follows: A SH Hall resistivity can be observed even in the absence of B , when a current is applied along the x -direction. A SH longitudinal resistivity can be induced along the x -direction upon the application of B . This can also be seen as the induction of second-order longitudinal magnetoresistance in a system due to the effect of geometric quantities. On the other hand, for a current along the y -direction, a SH Hall resistivity can be brought about upon the application of B . The SH longitudinal resistivity along the y -direction is zero, irrespective of the presence or absence of B (up to linear order in B). These observations highlight the intriguing asymmetry in the dependence on the magnetic field between the two directions. It is clear that the SH resistivities of this system are influenced by both geometric quantities and the underlying mirror symmetry, contributing to the distinct responses observed along the x and y directions.

VI. CONCLUSIONS

In this study, we investigated the linear and second-order NL current and voltage responses of a 2D gapped semi-Dirac system with merging Dirac nodes. We analyzed the system's response to a weak magnetic field, using the semiclassical Boltzmann formalism. Notably, the system possesses an intrinsic NL anomalous Hall conductivity, which can be attributed to the underlying mirror symmetry⁵⁹. The application of a magnetic field introduces three distinct contributions to the SH conductivity tensor, originating from geometric quantities: the combined effects of anomalous velocity and Lorentz force, the OMM, and the Berry curvature correction to the phase-space factor.

We have obtained exact analytical expressions for the linear and SH conductivities of the system, expressed in terms of complete elliptic integrals of the first and second kind, within the transport limit. Our findings have facilitated a comprehensive analysis of the conductivities and their dependence on Fermi energy and δ_0 . For $\delta_0 > 0$, the change in Fermi surface topology (from a single-connected Fermi surface for high Fermi energy to two Fermi surfaces for low Fermi energy) is also manifested in the behavior of both the obtained linear and SH conductivities. A small kink is observed at the saddle point $\gamma = 1$ for the fixed positive values of δ_0 which marks the transition between two different type of Fermi surfaces. We obtained approximate expressions for conductivities at low Fermi energy and explicitly showed their dependence on Fermi energy and δ_0 near the band edge.

We found that the geometric mean (ratio) of Drude conductivities in the x and y directions is independent of δ_0 for low (high) doping. We showed that the ratio of the anomalous velocity and Lorentz force-induced SH Hall conductivity to the SH anomalous Hall conductivity is independent of δ_0 and inversely related to Fermi energy. It is to be noted that in a time-reversal symmetric system, SH Drude conductivity vanishes which implies that the SH longitudinal magnetoconductivity arises solely due to geometric quantities.

We have also examined the zero-frequency current response generated at the second-order in the electric field. We have observed that the orientation of the NL dc current depends on the Fermi energy, magnetic field and polarization of electromagnetic wave. In the absence of magnetic field, the NL dc currents are oriented purely along the y -direction for x -polarized and low-frequency circularly polarized light ($\omega\tau \ll 1$), whereas they align along the x -direction for high-frequency circularly polarized light ($\omega\tau \gg 1$). It is worth noting that the NL dc current vanishes entirely for y -polarized light in absence of B . These orientations are predominantly governed by the underlying mirror symmetry of the system. In the presence of a magnetic field, the Fermi energy of the system serves as a control parameter for rotating the net NL dc current vector. Substantial rotations can be achieved by applying x -polarized and low-frequency circularly polarized light ($\omega\tau \ll 1$) compared to high-frequency circular polarization ($\omega\tau \gg 1$). However, no rotation is observed for y -polarized light. For y -polarized light, the NL dc current is consistently parallel or antiparallel to the x -axis. However, for x -polarized light, the NL DC current is nearly y -directed at high Fermi energies. In the high frequency limit, for circular polarization, the NL dc current aligns in a direction close to x -axis. Conversely, at low frequencies, the CPGE current vanishes and the NL dc current is directed close to the y -axis for high fermi energies. This conversion of applied ac electric field into DC current (rectification) in proposed semi-Dirac materials may hold applications for a wide range of technologies⁷¹.

We further study the SH magnetoresistivities of the system for two different orientations of current flow: (1) along x and (2) along y directions. For the current applied along the x -direction, the SH longitudinal resistivity scales linearly with the magnetic field, while SH Hall resistivity is independent of B in the lowest B -order. However, for the current applied along the y -direction, the SH longitudinal resistivity vanishes in both zeroth and linear order of B and SH Hall resistivity varies linearly with B in the lowest order. The predicted B -linear dependence of SH resistivities mainly arises from SH conductivities, which stem from band geometric quantities and underlying mirror symmetry of the system. Our results provide the platform for understanding the second-order NL magnetotransport induced by geometric quantities in an anisotropic 2D system undergoing a topological transition with merging of two Dirac points.

ACKNOWLEDGEMENTS

We would like to thank Kamal Das for useful discussions.

Appendix A: Linear current responses

In this appendix, we calculate the current responses linear in E and up to linear order in B . To obtain the NDF linear in E , we use the ansatz $f_1(t) = f_1^\omega e^{-i\omega t} + f_1^{\omega*} e^{i\omega t}$ in Eq. (3) and obtain

$$f_1^\omega = \frac{1}{2} \sum_{\eta=0}^{\infty} \left(\frac{\tau_\omega \hat{L}_B}{D} \right)^\eta \left(\frac{e\tau_\omega}{\hbar D} \mathbf{E} \cdot \nabla_{\mathbf{k}} \tilde{f}_{\text{eq}} \right), \quad (\text{A1})$$

where $\tau_\omega = \tau/(1 - i\omega\tau)$. The current responses linear in E can be expressed as $\mathbf{j}_1(t) = \mathbf{j}_{10}(t) + \mathbf{j}_{11}(t)$. The magnetic field independent current of fundamental frequency can be expressed as $\mathbf{j}_{10}(t) = \mathbf{j}_{10}^\omega e^{-i\omega t} + \mathbf{j}_{10}^{\omega*} e^{i\omega t}$, where we obtain

$$\mathbf{j}_{10}^\omega = -\frac{e^2}{2\hbar} \int [d\mathbf{k}] [\tau_\omega \mathbf{v}_{\mathbf{k}} (\mathbf{E} \cdot \nabla_{\mathbf{k}}) f_{\text{eq}} + (\mathbf{E} \times \boldsymbol{\Omega}) f_{\text{eq}}]. \quad (\text{A2})$$

The magnetic field independent conductivities take the following form

$$\sigma_{ab}^{(\text{D})} = -\frac{e^2 \tau_\omega}{2} \int [d\mathbf{k}] v_a v_b f'_{\text{eq}}. \quad (\text{A3})$$

$$\sigma_{ab}^{(\text{AHC})} = -\frac{e^2}{2\hbar} \varepsilon_{abd} \int [d\mathbf{k}] \Omega_d f_{\text{eq}}. \quad (\text{A4})$$

Equation (A3) refers to the Drude conductivity, while Eq. (A4) describes the intrinsic anomalous Hall conductivity which is independent of scattering time and vanishes for the TRS preserved system.

The magnetic field dependent current of fundamental frequency can be written as $\mathbf{j}_{11}(t) = \mathbf{j}_{11}^\omega e^{-i\omega t} + \mathbf{j}_{11}^{\omega*} e^{i\omega t}$, we get

$$\mathbf{j}_{11}^\omega = \frac{e^2}{2\hbar} \int [d\mathbf{k}] \left[(\mathbf{E} \times \boldsymbol{\Omega}) \epsilon_m f'_{\text{eq}} + \tau_\omega \mathbf{v}_{\mathbf{k}} \left\{ \frac{e}{\hbar} (\boldsymbol{\Omega} \cdot \mathbf{B}) (\mathbf{E} \cdot \nabla_{\mathbf{k}}) f_{\text{eq}} + (\mathbf{E} \cdot \nabla_{\mathbf{k}}) \epsilon_m f'_{\text{eq}} \right\} - \tau_\omega^2 \mathbf{v}_{\mathbf{k}} \hat{L} (\mathbf{E} \cdot \nabla_{\mathbf{k}}) f_{\text{eq}} \right], \quad (\text{A5})$$

where $\hat{L} = (e/\hbar)[(\mathbf{v}_{\mathbf{k}} \times \mathbf{B}) \cdot \nabla_{\mathbf{k}}]$. In the above expression, the terms proportional to τ vanish since Ω_k , v_k and ϵ_m are odd in the presence of TRS. The magnetic field-dependent conductivities which survive under TRS are given by

$$\sigma_{ab}^{(\text{L})} = -\frac{e^3 \tau_\omega^2 B}{2\hbar} \int [d\mathbf{k}] v_a (v_y \partial_{k_x} - v_x \partial_{k_y}) v_b f'_{\text{eq}}. \quad (\text{A6})$$

$$\sigma_{ab}^{(\text{OMM})} = \frac{e^2}{2\hbar} \varepsilon_{abd} \int [d\mathbf{k}] \Omega_d \epsilon_m f'_{\text{eq}}. \quad (\text{A7})$$

Equation (A6) represents the Lorentz force contribution (classical Hall effect), while Eq. (A7) describes the OMM-induced Hall effect.

Appendix B: Nonlinear DC current

In this Appendix, we provide the general expressions for the various contributions induced by Berry curvature and OMM to the NL DC current in the presence of magnetic field. These expressions are valid for all 2D systems

$$\begin{aligned} \mathbf{j}_{\text{NAL}}^{(0)} = & \frac{1}{(1 + \omega^2 \tau^2)^2} \left[(1 - \omega^2 \tau^2) \left\{ 2 \left(\chi_{xyy,0}^{(\text{NAL})} |E_y|^2 \hat{\mathbf{x}} + \chi_{yxx,0}^{(\text{NAL})} |E_x|^2 \hat{\mathbf{y}} \right) + \left(\chi_{xyx,0}^{(\text{NAL})} [E_y E_x^*]_+ \hat{\mathbf{x}} + \chi_{yxy,0}^{(\text{NAL})} [E_y E_x^*]_+ \hat{\mathbf{y}} \right) \right\} \right. \\ & \left. - 2i\omega\tau \left(\chi_{xyx,0}^{(\text{NAL})} [E_y E_x^*]_- \hat{\mathbf{x}} - \chi_{yxy,0}^{(\text{NAL})} [E_y E_x^*]_- \hat{\mathbf{y}} \right) \right]. \end{aligned} \quad (\text{B1})$$

The OMM contribution to the NL dc current can be calculated as

$$\begin{aligned} \mathbf{j}_{\text{OMM}}^{(0)} = & \frac{1}{1 + \omega^2 \tau^2} \left[2 \left(\chi_{xxx,0}^{(\text{OMM})} |E_x|^2 + \chi_{xyy,0}^{(\text{OMM})} |E_y|^2 \right) \hat{\mathbf{x}} + 2 \left(\chi_{yxx,0}^{(\text{OMM})} |E_x|^2 + \chi_{yyy,0}^{(\text{OMM})} |E_y|^2 \right) \hat{\mathbf{y}} \right. \\ & + \left(\chi_{xxy,0}^{(\text{OMM})} + \chi_{xyx,0}^{(\text{OMM})} \right) [E_y E_x^*]_+ \hat{\mathbf{x}} + \left(\chi_{yxy,0}^{(\text{OMM})} + \chi_{yyx,0}^{(\text{OMM})} \right) [E_y E_x^*]_+ \hat{\mathbf{y}} \\ & \left. - i\omega\tau \left\{ \left(\chi_{xyx,0}^{(\text{OMM})} - \chi_{xxy,0}^{(\text{OMM})} \right) [E_y E_x^*]_- \hat{\mathbf{x}} + \left(\chi_{yyx,0}^{(\text{OMM})} - \chi_{yxy,0}^{(\text{OMM})} \right) [E_y E_x^*]_- \hat{\mathbf{y}} \right\} \right], \end{aligned} \quad (\text{B2})$$

The NL dc current induced by the phase-space factor can be obtained as

$$\mathbf{j}_{\text{B}}^{(0)} = \mathbf{j}_{\text{OMM}}^{(0)} \left(\chi_{abc,0}^{(\text{OMM})} \rightarrow \chi_{abc,0}^{(\text{B})} \right), \quad (\text{B3})$$

where $\chi_{abc,0}^{(\text{NAL})} = \chi_{abc}^{(\text{NAL})}(\omega = 0)$, $\chi_{abc,0}^{(\text{OMM})} = \chi_{abc}^{(\text{OMM})}(\omega =$

and are presented in terms of the polarization of the electromagnetic wave.

The NL dc current emerging from the interplay of anomalous velocity and Lorentz force can be obtained as

$\chi_{abc,0}^{(\text{B})} = \chi_{abc}^{(\text{B})}(\omega = 0)$ are the corresponding SH conductivities given by Eqs. (9)-(11), respectively, for $\omega = 0$.

-
- ¹ K. S. Novoselov, A. K. Geim, S. V. Morozov, D. Jiang, Y. Zhang, S.V. Dubonos, I. V. Gregorieva and A. A. Firsov, Electric field effect in atomically thin carbon films, *Science* **306**, 666 (2004).
 - ² A. H. Castro Neto, F. Guinea, N. M. R. Peres, K. S. Novoselov, and A. K. Geim, The electronic properties of graphene, *Rev. Mod. Phys.* **81**, 109 (2009).
 - ³ A. Kobayashi, S. Katayama, Y. Suzumura, and H. Fukuyama, Massless Fermions in Organic Conductor, *J. Phys. Soc. Jpn.* **76**, 034711 (2007).
 - ⁴ M. O. Goerbig, J.-N. Fuchs, G. Montambaux, and F. Piéchon, Tilted anisotropic Dirac cones in quinoid-type graphene and α -(BEDT-TTF)₂I₃, *Phys. Rev. B* **78**, 045415 (2008).
 - ⁵ Y. Suzumura and A. Kobayashi, Berry Curvature of the Dirac Particle in α -(BEDT-TTF)₂I₃, *J. Phys. Soc. Jpn.* **80**, 104701 (2011).
 - ⁶ M. Hirata, K. Ishikawa, G. Matsuno, A. Kobayashi, K. Miyagawa, M. Tamura, C. Berthier, and K. Kanoda, Anomalous spin correlations and excitonic instability of interacting 2D Weyl fermions, *Science* **358**, 1403 (2017).
 - ⁷ X. F. Zhou, X. Dong, A. R. Oganov, Q. Zhu, Y. Tian, and H. T. Wang, Semimetallic Two-Dimensional Boron Allotrope with Massless Dirac Fermions, *Phys. Rev. Lett.* **112**, 085502 (2014).
 - ⁸ A. D. Zabolotskiy and Y. E. Lozovik, Strain-induced pseudomagnetic field in the Dirac semimetal borophene, *Phys. Rev. B* **94**, 165403 (2016).
 - ⁹ T. G. Pedersen, Nonlinear optical response of relativistic energy bands: Application to phosphorene, *Phys. Rev. B* **95**, 235419 (2017).
 - ¹⁰ K. Maekawa, M. Takizawa, H. Wadati, T. Yoshida, A. Fujimori, H. Kumigashira, M. Oshima, Y. Muraoka, Y. Nagao, and Z. Hiroi, Photoemission study of TiO₂/VO₂ interfaces, *Phys. Rev. B* **76**, 115121 (2007).
 - ¹¹ S. Bittner, B. Dietz, M. Miski-Oglu, P. Oria Iriarte, A. Richter, and F. Schäfer, Observation of a Dirac point in microwave experiments with a photonic crystal modeling graphene, *Phys. Rev. B* **82**, 014301 (2010).
 - ¹² M. Polini, F. Guinea, M. Lewenstein, H. C. Manoharan, and V. Pellegrini, Artificial honeycomb lattices for electrons, atoms and photons, *Nat. Nanotech.* **8**, 625 (2013).
 - ¹³ M. Bellec, U. Kuhl, G. Montambaux, and F. Mortessagne, Topological Transition of Dirac Points in a Microwave Experiment, *Phys. Rev. Lett.* **110**, 033902 (2013).
 - ¹⁴ T. Jacqmin, I. Carusotto, I. Sagnes, M. Abbarchi, D. D. Solnyshkov, G. Malpuech, E. Galopin, A. Lemaitre, J. Bloch, and A. Amo, Direct Observation of Dirac Cones and a Flatband in a Honeycomb Lattice for Polaritons, *Phys. Rev. Lett.* **112**, 116402 (2014).

- ¹⁵ S.-L. Zhu, B. Wang and L.-M. Duan, Simulation and Detection of Dirac Fermions with Cold Atoms in an Optical Lattice, *Phys. Rev. Lett.* **98**, 260402 (2007).
- ¹⁶ J.-M. Hou, W.-X. Yang and X.-J. Liu, Massless Dirac Fermions in a Square Optical Lattice, *Phys. Rev. A* **79**, 043621 (2009).
- ¹⁷ B. Wunsch, F. Guinea, and F. Sols, Dirac-point engineering and topological phase transitions in honeycomb optical lattices, *New J. Phys.* **10**, 103027 (2008).
- ¹⁸ Y. Hasegawa, R. Konno, H. Nakano, and M. Kohmoto, Zero modes of tight-binding electrons on the honeycomb lattice, *Phys. Rev. B* **74**, 033413 (2006).
- ¹⁹ G. Montambaux, F. Piéchon, J.-N. Fuchs, and M. O. Goerbig, Merging of Dirac points in a two-dimensional crystal, *Phys. Rev. B* **80**, 153412 (2009).
- ²⁰ G. Montambaux, F. Piéchon, J.-N. Fuchs, and M. O. Goerbig, A universal hamiltonian for motion and merging of dirac points in a two-dimensional crystal, *Eur. Phys. J. B* **72**, 509 (2009).
- ²¹ V. Pardo, and W. E. Pickett, Half-Metallic Semi-Dirac-Point Generated by Quantum Confinement in TiO_2/VO_2 Nanostructures, *Phys. Rev. Lett.* **102**, 166803 (2009).
- ²² Y. Wu, A semi-Dirac point and an electromagnetic topological transition in a dielectric photonic crystal, *Opt. Express* **22**, 1906 (2014).
- ²³ L. Tarruell, D. Greif, T. Uehlinger, G. Jotzu, and T. Esslinger, Creating, moving and merging Dirac points with a Fermi gas in a tunable honeycomb lattice, *Nature* **483**, 10871 (2012).
- ²⁴ J. Kim, S. S. Baik, S. H. Ryu, Y. Sohn, S. Park, B.-G. Park, J. Denlinger, Y. Yi, H. J. Choi, and K. S. Kim, Observation of tunable band gap and anisotropic Dirac semimetal state in black phosphorus, *Science* **349**, 723 (2015).
- ²⁵ P. Adroguer, D. Carpentier, G. Montambaux and E. Orignac, Diffusion of Dirac fermions across a topological merging transition in two dimensions, *Phys. Rev. B* **93**, 125113 (2016).
- ²⁶ A. Mawrie and B. Muralidharan, Direction-dependent giant optical conductivity in two-dimensional semi-Dirac materials, *Phys. Rev. B* **99**, 075415 (2019).
- ²⁷ J. P. Carbotte and E. J. Nicol, Signatures of merging Dirac points in optics and transport, *Phys. Rev. B* **100**, 035441 (2019).
- ²⁸ J. Jang, S. Ahn, and H. Min, Optical conductivity of black phosphorus with a tunable electronic structure, *2D Materials* **6**, 025029 (2019).
- ²⁹ D. O. Oriekhov and V. P. Gusynin, Optical conductivity of semi-Dirac and pseudospin-1 models: Zitterbewegung approach, *Phys. Rev. B* **106**, 115143 (2022).
- ³⁰ P. Dietl, F. Piéchon, and G. Montambaux, New Magnetic Field Dependence of Landau Levels in a Graphenelike Structure, *Phys. Rev. Lett.* **100**, 236405 (2008).
- ³¹ P. Delplace, and G. Montambaux, Semi-Dirac point in the Hofstadter spectrum, *Phys. Rev. B* **82**, 035438 (2010).
- ³² X. Zhou, W. Chen, and X. Zhu, Anisotropic magneto-optical absorption and linear dichroism in two-dimensional semi-Dirac electron systems, *Phys. Rev. B* **104**, 235403 (2021).
- ³³ P. K. Pyatkovskiy and T. Chakraborty, Dynamical polarization and plasmons in a two-dimensional system with merging Dirac points, *Phys. Rev. B* **93**, 085145 (2016).
- ³⁴ P. Sinha, S. Murakami and S. Basu, Quantum Hall studies of a semi-Dirac nanoribbon, *Phys. Rev. B* **102**, 085416 (2020).
- ³⁵ K. Saha, Photoinduced Chern insulating states in semi-Dirac materials, *Phys. Rev. B* **94**, 081103(R) (2016).
- ³⁶ S. Mondal and S. Basu, Topological phases of a semi-Dirac Chern insulator in the presence of extended range hopping, *Phys. Rev. B* **105**, 235441 (2022).
- ³⁷ D. Xiao, M.-C. Chang, and Q. Niu, Berry phase effects on electronic properties, *Rev. Mod. Phys.* **82**, 1959 (2010).
- ³⁸ J. E. Moore and J. Orenstein, Confinement-Induced Berry Phase and Helicity-Dependent Photocurrents, *Phys. Rev. Lett.* **105**, 026805 (2010).
- ³⁹ F. D. M. Haldane, Berry Curvature on the Fermi Surface: Anomalous Hall Effect as a Topological Fermi-Liquid Property, *Phys. Rev. Lett.* **93**, 206602 (2004).
- ⁴⁰ N. A. Sinitsyn, Semiclassical theories of the anomalous Hall effect, *Journal of Physics: Condensed Matter* **20**, 023201 (2008).
- ⁴¹ A. A. Burkov and L. Balents, Weyl Semimetal in a Topological Insulator Multilayer, *Phys. Rev. Lett.* **107**, 127205, (2011).
- ⁴² T. Qin, Q. Niu and J. Shi, Energy Magnetization and the Thermal Hall Effect, *Phys. Rev. Lett.* **107**, 236601 (2011).
- ⁴³ P. Goswami and S. Tewari, Axionic field theory of (3 + 1)-dimensional Weyl semimetals, *Phys. Rev. B* **88**, 245107 (2013).
- ⁴⁴ S. Nandy, G. Sharma, A. Taraphder and S. Tewari, Chiral Anomaly as the Origin of the Planar Hall Effect in Weyl Semimetals, *Phys. Rev. Lett.* **119**, 176804 (2017).
- ⁴⁵ A. A. Burkov, Giant planar Hall effect in topological metals, *Phys. Rev. B* **96**, 041110 (2017).
- ⁴⁶ K.-S. Kim, H.-J. Kim and M. Sasaki, Boltzmann equation approach to anomalous transport in a Weyl metal, *Phys. Rev. B* **89**, 195137 (2014).
- ⁴⁷ H. Zhou, C. Xiao, and Q. Niu, Valley-contrasting orbital magnetic moment induced negative magnetoresistance, *Phys. Rev. B* **100**, 041406 (2019).
- ⁴⁸ I. Sodemann and L. Fu, Quantum Nonlinear Hall Effect Induced by Berry Curvature Dipole in Time-Reversal Invariant Materials, *Phys. Rev. Lett.* **115**, 216806 (2015).
- ⁴⁹ C. Xiao, Z. Z. Du, and Q. Niu, Theory of nonlinear Hall effects: Modified semiclassics from quantum kinetics, *Phys. Rev. B* **100**, 165422 (2019).
- ⁵⁰ K. Kang, T. Li, E. Sohn, J. Shan, and K. F. Mak, Nonlinear anomalous Hall effect in few-layer WTe_2 , *Nature Materials* **18**, 324-328 (2019).
- ⁵¹ J. Son, K.-H. Kim, Y. H. Ahn, H.-W. Lee, and J. Lee, Strain Engineering of the Berry Curvature Dipole and Valley Magnetization in Monolayer MoS_2 , *Phys. Rev. Lett.* **123**, 036806 (2019).
- ⁵² Y. Zhang, Y. Sun, and B. Yan, Berry curvature dipole in Weyl semimetal materials: An *ab initio* study, *Phys. Rev. B* **97**, 041101 (2018).
- ⁵³ Z. Z. Du, C. M. Wang, H.-Z. Lu, and X. C. Xie, Band Signatures for Strong Nonlinear Hall Effect in Bilayer WTe_2 , *Phys. Rev. Lett.* **121**, 266601 (2018).
- ⁵⁴ J. I. Facio, D. Efremov, K. Koepf, J.-S. You, I. Sodemann, and J. van den Brink, Strongly Enhanced Berry Dipole at Topological Phase Transitions in BiTeI , *Phys. Rev. Lett.* **121**, 246403 (2018).
- ⁵⁵ Z. Z. Du, C. M. Wang, S. Li, H.-Z. Lu, and X. C. Xie, Disorder-induced nonlinear Hall effect with time-reversal symmetry, *Nature Communications* **10**, 3047 (2019).
- ⁵⁶ B. T. Zhou, C.-P. Zhang, and K. T. Law, Highly Tunable Nonlinear Hall Effects Induced by Spin-Orbit Couplings in Strained Polar Transition-Metal Dichalcogenides, *Phys.*

- Rev. Applied **13**, 024053 (2020).
- ⁵⁷ Z. Z. Du, C. M. Wang, H.-P. Sun, H.-Z. Lu, and X. C. Xie, Quantum theory of the nonlinear Hall effect, *Nature Communications* **12**, 5038 (2021).
- ⁵⁸ R. Battilomo, N. Scopigno, and C. Ortix, Berry Curvature Dipole in Strained Graphene: A Fermi Surface Warping Effect, *Phys. Rev. Lett.* **123**, 196403 (2019).
- ⁵⁹ S. S. Samal, S. Nandy, and K. Saha, Nonlinear transport without spin-orbit coupling or warping in two-dimensional Dirac semimetals, *Phys. Rev. B* **103**, L201202 (2021).
- ⁶⁰ G. Sundaram and Q. Niu, Wave-packet dynamics in slowly perturbed crystals: Gradient corrections and Berry-phase effects, *Phys. Rev. B* **59**, 14915 (1999).
- ⁶¹ T. Morimoto, S. Zhong, J. Orenstein and J. E. Moore, Semiclassical theory of nonlinear magneto-optical responses with applications to topological Dirac/Weyl semimetals, *Phys. Rev. B* **94** 245121 (2016).
- ⁶² M. C. Chang, and Q. Niu, Berry phase, hyperorbits, and the Hofstadter spectrum: Semiclassical dynamics in magnetic Bloch bands, *Phys. Rev. B* **53**, 7010 (1996).
- ⁶³ D. Xiao, W. Yao, and Q. Niu, Valley-Contrasting Physics in Graphene: Magnetic Moment and Topological Transport, *Phys. Rev. Lett.* **99**, 236809 (2007).
- ⁶⁴ N. W. Ashcroft and N. D. Mermin, *Solid State Physics, HRW International Editions* (Holt, Rinehart and Winston, New York, 1976).
- ⁶⁵ J. M. Ziman, *Electrons and Phonons: The Theory of Transport Phenomena in Solids* (Clarendon Press, Oxford, 1967).
- ⁶⁶ H. K. Pal and D. L. Maslov, Necessary and sufficient condition for longitudinal magnetoresistance, *Phys. Rev. B* **81**, 214438 (2010).
- ⁶⁷ Q. Ma, S.-Y. Xu, H. Shen, D. MacNeill, V. Fatemi, T.-R. Chang, A. M. Mier Valdivia, S. Wu, Z. Du, C.-H. Hsu, S. Fang, Q. D. Gibson, K. Watanabe, T. Taniguchi, R. J. Cava, E. Kaxiras, H.-Z. Lu, H. Lin, L. Fu, N. Gedik, and P. Jarillo-Herrero, Observation of the nonlinear Hall effect under time-reversal-symmetric conditions, *Nature* **565**, 337 (2019).
- ⁶⁸ S. Lahiri, T. Bhore, K. Das, and A. Agarwal, Nonlinear magnetoresistivity in two-dimensional systems induced by Berry curvature, *Phys. Rev. B* **105**, 045421 (2022).
- ⁶⁹ P. He, S. S.-L. Zhang, D. Zhu, Y. Liu, Y. Wang, J. Yu, G. Vignale, and H. Yang, Bilinear magnetoelectric resistance as a probe of three-dimensional spin texture in topological surface states, *Nat. Phys.* **14**, 495 (2018).
- ⁷⁰ P. He, S. S.-L. Zhang, D. Zhu, S. Shi, O. G. Heinonen, G. Vignale, and H. Yang, Nonlinear Planar Hall Effect, *Phys. Rev. Lett.* **123**, 016801 (2019).
- ⁷¹ H. Isobe, S.-Y. Xu, and L. Fu, High-frequency rectification via chiral Bloch electrons, *Sci. Adv.* **6**, eaay2497 (2020).